

Extreme nonequilibrium electrophoresis of an ion-selective microgranuleG. S. Ganchenko,¹ E. A. Frants,^{2,3,4} V. S. Shelistov,¹ N. V. Nikitin,⁵ S. Amiroudine,⁴
and E. A. Demekhin^{1,2,5,*}¹*Laboratory of Micro- and Nanoscale Electro- and Hydrodynamics, Financial University,
Krasnodar 350051, Russian Federation*²*Department of Mathematics and Computer Science, Financial University,
Krasnodar 350051, Russian Federation*³*Department of Applied Mathematics, Kuban State University, Krasnodar 350040, Russian Federation*⁴*TREFLE, Institut de Mécanique et d'Ingénierie, UMR No. 5295, CNRS, University of Bordeaux,
16 Avenue Pey-Berland, Pessac Cedex, France*⁵*Laboratory of General Aeromechanics, Institute of Mechanics, Moscow State University,
Moscow 119192, Russian Federation*

(Received 11 September 2018; published 16 April 2019)

We investigate the electrophoresis of an ion-selective microgranule in an electrolyte solution. A semianalytical analysis of a small length of the electric double layer as well as overlimiting and extreme overlimiting currents is complemented by the direct numerical study of the full nonstationary Nernst-Planck-Poisson-Stokes system, with the corresponding boundary and initial conditions. Our results are in reasonably good agreement with the available experimental data. Moreover, they can be used to modify Dukhin's formula for the electrophoretic velocity. A steady-state solution is observed for moderate electric fields. Three boundary layers, nested inside each other, are formed in this solution as follows: an electric double layer, a space-charge region, and a thin diffusion layer. Only the electric double layer is present in the area of the outgoing ion flux. This flux generates a jet of high electric conductivity. Increasing the external field makes this jet narrower, but its conductivity increases. At the point on the granule surface where the ion flux vanishes, a separation of the diffusion boundary layer occurs. For sufficiently strong fields, the steady-state solution loses stability. Instability arises in the diffusion layer region but manifests itself in other regions. In particular, it generates electrokinetic microvortices. Two kinds of microvortices are found: large steady Dukhin-Mishchuk vortices and electrokinetic vortices that propagate from the pole of the particle towards the Dukhin-Mishchuk vortices. At small supercriticality, the oscillations of the unknowns are periodic, but increasing the external field makes the flow chaotic in the Feigenbaum scenario fashion.

DOI: [10.1103/PhysRevFluids.4.043703](https://doi.org/10.1103/PhysRevFluids.4.043703)**I. INTRODUCTION**

The motion of charged micro- and nanoparticles and macromolecules under the influence of an external electric field is addressed in the present work. Electrophoresis is a fundamental phenomenon in theoretical physics with ever-increasing applications in microfluidics [1,2] and bioanalysis [3], enabling the efficient manipulation of charged particles in microfluidic devices. The applications include laboratory-on-a-chip technologies, DNA transport, the separation of dispersed micro- and nanoparticles and cells [4], and so on.

*edemekhi@gmail.com

One of the most promising applications of ion-selective particles is medical analysis. The small charged molecules of different peptides can act as biomarkers for certain diseases. The problem is that their concentrations in a biological fluid are extremely low (below pg/ml), which makes it difficult to identify these molecules [5]. Wang *et al.* [6] showed that a sixth-order enhancement in the ion concentration (superconcentration) can be achieved locally within the double layer if the particle is permeable to ions. This effect may be the key to the early detection of various diseases by biomarkers. Another application of ion-selective particles was stated by Dukhin and Mishchuk [7,8] for electro dialysis intensification. An increase of the electric field leads to an increase of the current until the current saturation is observed (so-called limiting current). The limiting current regime constrains the electro dialysis efficiency. The manifestation of electrokinetic phenomena of the second kind allows avoiding the limiting current. For this purpose, Dukhin [7] proposed a mixed-bed ion exchanger, in which a layer of the cation-exchange granule alternates with a layer of a cation-exchange planar membrane.

It should be noted that this phenomenon strongly depends on the properties of the particle-electrolyte surface. Distinct results have been obtained for different kinds of particles in the literature, particularly between charged dielectric and ion-selective particles.

The study of the electrophoresis of dielectric particles, which are impermeable both for cations and for anions, began more than a century ago with the works of Helmholtz [9] and Smoluchowski [10], who studied the electrophoresis and electro-osmosis of dielectric particles. They obtained a simple mathematical description of these phenomena, including a formula for the electrophoretic velocity under the assumption of a thin electric double layer (EDL) and a weak external electric field,

$$\tilde{u}_\infty = \frac{\tilde{\varepsilon}\tilde{\zeta}}{\tilde{\mu}}\tilde{E}_\infty. \quad (1)$$

The velocity \tilde{u}_∞ is linearly proportional to the applied electric field \tilde{E}_∞ and the zeta potential $\tilde{\zeta}$ and is inversely proportional to the viscosity $\tilde{\mu}$. Here $\tilde{\varepsilon}$ is the dielectric permittivity of the medium around the particle. It can be seen that there is no dependence of the velocity on the particle size. The electrophoresis described by the relation (1) is called electrophoresis of the first kind or linear electrophoresis.

After the works of Helmholtz and Smoluchowski, a whole series of experimental and theoretical papers were devoted to the electrophoresis of dielectric particles. The effects of the surface conductance, the finite thickness of the EDL, the surface charge, and transition processes were investigated by Van Der Put and Bijsterbosch [11], Wiersema *et al.* [12], O'Brien and White [13], Bazant [14], and Lyklema [15].

Hamed and Yariv [16,17] used a weak-field expansion to analyze the steady-state electrokinetic flow around an ideally polarized spherical nanoparticle for the case of a large Debye thickness in relation to the particle size. Yariv and Davis [18] used a macroscale model that was proposed by Yossifon *et al.* [19] to analyze electrokinetic flows around dielectric surfaces for a thin EDL. The authors developed and analyzed electrokinetic effects, wherein solid polarization modifies the ζ -potential distribution. They found that nonlinearity had a hindering effect.

Smoluchowski's theory predicts a linear enhancement of the velocity with the growth of the ζ potential, but this dependence was derived for small- ζ -potential values and thus is unreliable for moderate values [20,21]. Schnitzer and Yariv [20] proved analytically that this relation is still reliable for moderate- ζ potentials but is not valid for larger ones. In their next study, Schnitzer and Yariv [21] presented a generic analysis of electrokinetic transport around highly charged dielectric solids in a thin EDL, which was not restricted to weak fields. In the nonlinear regime, non-Smoluchowski electrophoretic mobilities should be used. Schnitzer *et al.* [22] generalized the results of the work in Ref. [21] to large- ζ potentials, when surface conduction became significant in thin EDL electrokinetic transport.

The behavior of a charge-selective granule, which allows only one kind of ions, i.e., cations or anions, to penetrate through its surface is very different from the behavior of the dielectric particles. The mathematical formulation of the problem near a planar charge-selective solid, when

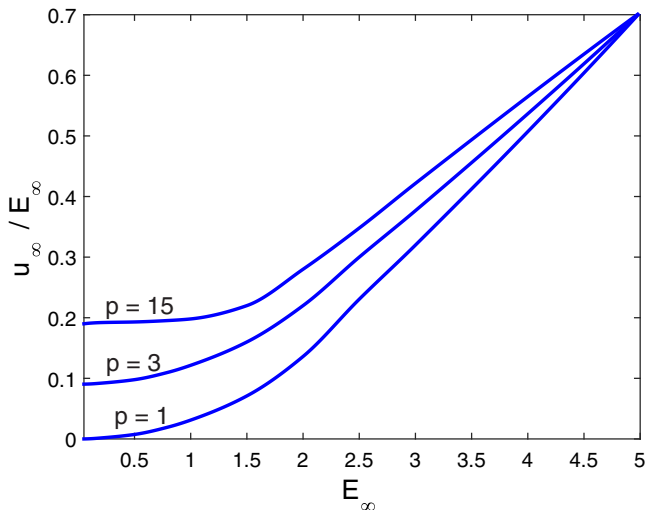
two charge-selective surfaces were separated by a layer of electrolyte, was provided by Rubinstein and Shtilman [23]; a one-dimensional quiescent solution was found where electromigration was balanced by diffusion. This process is accompanied by the flux of ions through the membrane surface, so this is a nonequilibrium phenomenon. Two kinds of regimes were distinguished. (a) At a small drop of the potential, the influence of the ion flux can be neglected and the regime is practically in equilibrium or, to be more precise, in quasiequilibrium (the so-called underlimiting currents). The EDL is formed near the charge-selective surfaces. (b) If the external field increases, then the ion flux through the surface cannot be neglected. Moreover, it dominates other processes and a nonequilibrium structure, the space-charge region (SCR), appears from the quasiequilibrium structure of the EDL. This nonequilibrium regime is called the limiting current regime. The formulation [23] was successfully used by Rubinstein and Zaltzman [24] to study analytically the electrokinetic instability for the extreme overlimiting currents by Zaltzman and Rubinstein [25], to develop a universal theory of the electrokinetic instability that is uniformly valid for both quasiequilibrium and nonequilibrium conditions. Demekhin *et al.* [26–28] developed a numerical approach for the linear and nonlinear electrokinetic instability. In works by Pham *et al.* [29] and Druzgalski *et al.* [30], the direct numerical simulation of the mentioned processes near a planar charge-selective surface was fulfilled.

A charge-selective microgranule can be considered as a sophisticated type of electric membrane. In particular, in contrast to the planar geometry, a curved interface (along with the electrokinetic instability) is one of the conditions for the nonlinear phenomena to appear. Experimental investigations of the electro-osmosis and electrophoresis of charge-selective granules were conducted in the studies by Mishchuk and co-workers [31–33] and Barany [34]. Despite the differences between the problems of electrophoresis and of electrokinetics near planar membranes, they also have similarities. Dukhin and Mishchuk and co-workers found two kinds of electrophoresis of charge-selective granules. At small external fields, the granule velocity is proportional to the field strength and independent of the granule size, as in the classical electrophoresis at a small electric field, so it is the electrophoresis of the first kind connected with the quasiequilibrium EDL near the surface. With increasing external field the behavior of the particle becomes of nonequilibrium type (the influence of the ion flux now plays a dominant role) and the particle mobility now depends on the electric field. The nonequilibrium electro-osmosis related to the SCR is called electro-osmosis of the second kind, as described by Dukhin and Mishchuk and co-workers (see [7,31]). Numerous experimental data were presented by the researchers. However, the main result of these works is that the linear dependence of the electrophoretic velocity on the electric field at sufficiently large field breaks down and changes to a quadratic dependence (see [7])

$$\tilde{u}_\infty = 2 \frac{\tilde{\alpha} \tilde{E}_\infty^2}{\tilde{\mu}}. \quad (2)$$

Moreover, in contrast to the relation (1), there is now a dependence of the velocity on the granule size $\tilde{\alpha}$. Dukhin named this electrophoresis of the second kind, or nonlinear electrophoresis.

In the work by Yariv [35] the behavior of an ion-selective particle was for the first time investigated for a small Debye layer and weak external field, using asymptotic methods. In our recent work [36] we investigate numerically and asymptotically the case of weak and moderate electric fields and a transition zone from the electrophoresis of the first and the second kind. It was shown that at a sufficiently large electric field, the electrophoretic velocity and other variables become independent of the properties of the fabric of the ion-exchange membrane. In our formulation, this means independence from the surface charge p . In Fig. 1 the mobility of an ion-exchange membrane is plotted as a function of the surface charge p (see [36] for details) (the variables are in dimensionless form, here $u_\infty = \frac{\tilde{u}_\infty \tilde{\alpha}}{\tilde{D}}$ and $E_\infty = \frac{\tilde{E}_\infty \tilde{\alpha}}{\tilde{\Phi}_0}$, where $\tilde{\alpha}$ is the radius of the sphere, \tilde{D} is the coefficient of diffusion of ions, and $\tilde{\Phi}_0$ is the thermal potential); at $E_\infty > 5$ dependences for the mobilities for different p converge to one point. In other words, at sufficiently high electric fields, the electrokinetic effects are controlled by the ion flux through the

FIG. 1. Mobility vs E_∞ for different p .

particle and the phenomenon acquires a nonequilibrium behavior. In the work of [36], using an asymptotic method for a small external field and small Debye number, an analytical relation for the electrophoretic velocity was derived,

$$\tilde{u}_\infty = \frac{\tilde{\epsilon}\tilde{\zeta}}{2\tilde{\mu}} \left(1 - 0.11 \frac{\tilde{\zeta}}{\tilde{\Phi}_0} \right) \tilde{E}_\infty, \quad (3)$$

where $\tilde{\Phi}_0$ is the thermal potential. This is different from the Helmholtz-Smoluchowski formula (1), although the velocity is proportional to the electric field. For a small and moderate electric field, our theoretical results are in good agreement with experiments [31–34].

The present work addresses the electrophoresis of the ion-selective microgranule for the nonequilibrium and extreme nonequilibrium conditions. The investigation is fulfilled by direct numerical simulation of the Nernst-Planck-Poisson-Stokes system along with a semianalytical approach.

II. FORMULATION

We consider a spherical solid microgranule with a semiselective ion-exchange surface, which is impermeable to one kind of ions, without loss of generality, anions, with a radius \tilde{a} , suspended in an infinitely extending electrolyte solution. A symmetric (valence or charge number $z^+ = -z^- = 1$) binary electrolyte with the diffusivity of cations and anions \tilde{D} , the dynamic viscosity of liquid $\tilde{\mu}$, and the electric permittivity $\tilde{\epsilon}$ is considered. The microparticle is subjected to an electric field \tilde{E}_∞ , which induces the electrophoretic velocity \tilde{u}_∞ . Notation with a tilde is used for the dimensional variables, as opposed to their dimensionless counterparts without a tilde. We assume an axisymmetric problem in spherical polar coordinates (r, θ) (see Fig. 2).

The characteristic quantities to make the system dimensionless are as follows: \tilde{a} , the radius of the particle; $\frac{\tilde{a}^2}{\tilde{D}}$, time; $\frac{\tilde{D}}{\tilde{a}}$, velocity; $\tilde{\mu}$, dynamic viscosity; $\frac{\tilde{\mu}\tilde{D}}{\tilde{a}^2}$, pressure; $\tilde{\Phi}_0 = \frac{\tilde{R}\tilde{T}}{\tilde{F}}$, thermal potential; \tilde{c}_∞ , unperturbed ion concentration far away from the particle; and $\frac{\tilde{D}\tilde{F}\tilde{c}_\infty}{\tilde{a}}$, electric current. Here \tilde{F} is the Faraday constant, \tilde{R} is the universal gas constant, and \tilde{T} is the absolute temperature.

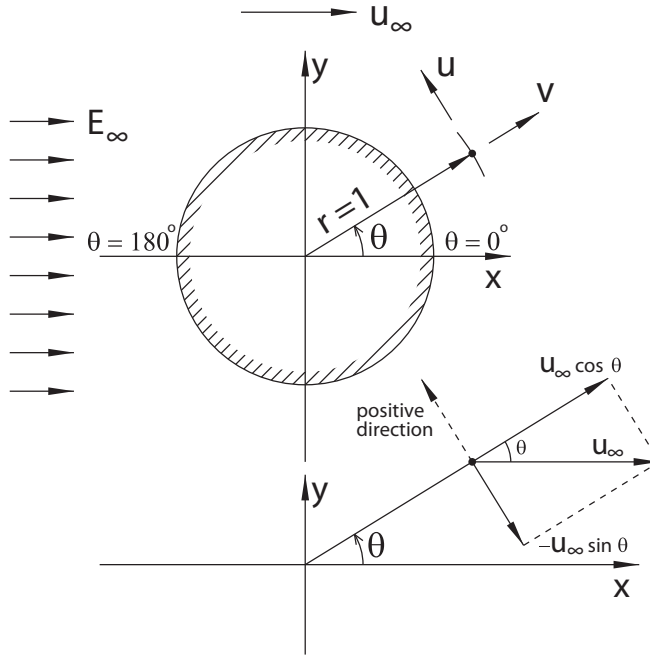


FIG. 2. Schematic of the flow near the granule under the external electric field E_∞ and the fluid flow velocity u_∞ at infinity, directed along the x axis. The electrophoretic velocity of the particle is in the opposite direction. In the spherical polar system $x = r \cos \theta$ and $y = r \sin \theta$, $u = u_\theta$ is the tangential velocity at the particle surface and $v = u_r$ is the normal velocity at the particle surface. At the comoving reference frame, the far-field velocity condition is $u \rightarrow -u_\infty \sin \theta$ and $v \rightarrow u_\infty \cos \theta$.

The problem is described by the nondimensional equations for the ion transport,

$$\begin{aligned} \frac{\partial c^+}{\partial t} + u \frac{1}{r} \frac{\partial c^+}{\partial \theta} + v \frac{\partial c^+}{\partial r} = & \left[\frac{1}{r^2 \sin \theta} \frac{\partial}{\partial \theta} \left(\sin \theta c^+ \frac{\partial \varphi}{\partial \theta} \right) + \frac{1}{r^2} \frac{\partial}{\partial r} \left(r^2 c^+ \frac{\partial \varphi}{\partial r} \right) \right] \\ & + \left[\frac{1}{r^2 \sin \theta} \frac{\partial}{\partial \theta} \left(\sin \theta \frac{\partial c^+}{\partial \theta} \right) + \frac{1}{r^2} \frac{\partial}{\partial r} \left(r^2 \frac{\partial c^+}{\partial r} \right) \right], \end{aligned} \quad (4)$$

$$\begin{aligned} \frac{\partial c^-}{\partial t} + u \frac{1}{r} \frac{\partial c^-}{\partial \theta} + v \frac{\partial c^-}{\partial r} = & - \left[\frac{1}{r^2 \sin \theta} \frac{\partial}{\partial \theta} \left(\sin \theta c^- \frac{\partial \varphi}{\partial \theta} \right) + \frac{1}{r^2} \frac{\partial}{\partial r} \left(r^2 c^- \frac{\partial \varphi}{\partial r} \right) \right] \\ & + \left[\frac{1}{r^2 \sin \theta} \frac{\partial}{\partial \theta} \left(\sin \theta \frac{\partial c^-}{\partial \theta} \right) + \frac{1}{r^2} \frac{\partial}{\partial r} \left(r^2 \frac{\partial c^-}{\partial r} \right) \right]; \end{aligned} \quad (5)$$

the Poisson equation for electric potential φ ,

$$\frac{v^2}{r^2} \left[\frac{\partial}{\partial r} \left(r^2 \frac{\partial \varphi}{\partial r} \right) + \frac{1}{\sin \theta} \frac{\partial}{\partial \theta} \left(\sin \theta \frac{\partial \varphi}{\partial \theta} \right) \right] = c^- - c^+ \equiv -\rho; \quad (6)$$

and the Stokes equations for creeping flow,

$$-\frac{1}{r} \frac{\partial \Pi}{\partial \theta} + \frac{\partial^2 u}{\partial r^2} + \frac{2}{r} \frac{\partial u}{\partial r} + \frac{1}{r^2} \frac{\partial^2 u}{\partial \theta^2} + \frac{\cot \theta}{r^2} \frac{\partial u}{\partial \theta} - \frac{u}{r^2 \sin^2 \theta} + \frac{2}{r^2} \frac{\partial v}{\partial \theta} = \rho \frac{1}{r} \frac{\partial \varphi}{\partial \theta}, \quad (7)$$

$$-\frac{\partial \Pi}{\partial r} + \frac{\partial^2 v}{\partial r^2} + \frac{2}{r} \frac{\partial v}{\partial r} + \frac{1}{r^2} \frac{\partial^2 v}{\partial \theta^2} - \frac{2v}{r^2} + \frac{\cot \theta}{r^2} \frac{\partial v}{\partial \theta} - \frac{2u}{r^2} \cot \theta - \frac{2}{r^2} \frac{\partial u}{\partial \theta} = \rho \frac{1}{r} \frac{\partial \varphi}{\partial r}, \quad (8)$$

$$\frac{\partial}{\partial \theta} [\sin(\theta)ru] + \frac{\partial}{\partial r} [\sin(\theta)r^2v] = 0. \quad (9)$$

Here (u, v) are the velocity components, c^+ and c^- are the molar concentrations of cations and anions, respectively, Π is the pressure, φ is the electric potential, and ρ is the space-charge density.

The problem is considered in a particle-fixed frame. The dimensionless parameter ν is the Debye number, which is the ratio of the Debye length $\tilde{\lambda}_D$ to the granule radius \tilde{a} ($\nu \ll 1$ is a small parameter of the problem when a thin EDL is considered),

$$\nu = \frac{\tilde{\lambda}_D}{\tilde{a}}, \quad \tilde{\lambda}_D = \left(\frac{\tilde{\varepsilon} \tilde{\Phi}_0}{\tilde{F} \tilde{c}_\infty} \right)^{1/2},$$

and \varkappa is a coupling coefficient between the hydrodynamics and electrostatics,

$$\varkappa = \frac{\tilde{\varepsilon} \tilde{\Phi}_0^2}{\tilde{\mu} \tilde{D}}.$$

This quantity characterizes the physical properties of the electrolyte solution and is fixed for a given liquid and electrolyte.

This system is complemented by the proper boundary conditions (BCs). On the particle surface, for $r = 1$, these conditions are

$$c^+ = p, \quad c^- \frac{\partial \varphi}{\partial r} - \frac{\partial c^-}{\partial r} = 0, \quad \varphi = 0, \quad u = v = 0. \quad (10)$$

The first BC in Eq. (10) was introduced in the paper by Rubinstein and Shtilman [23] (see also [24,25]). To better understand this BC, let us consider the structure of the membrane. The cation-exchange membrane is an organic polymer that consists of a matrix and pores. In the matrix, the anions c_a are fixed and immobile, which creates a fixed membrane charge p ($c_a = p$). When the membrane is placed in the electrolyte without any electrical field, the pores are filled with an electrolyte and ions of the opposite sign (c^+) accumulate in them. Moreover, their number is practically equal to the charge of the membrane ($c^+ = p$); that is, the membrane as a whole is screened from the inside. If the membrane charge is large enough ($p \gg 1$), then it is more difficult for external forces to change the number of cations inside the membrane, so $c^+ = p$ can be taken inside the membrane and at its surface with the electrolyte [see Eq. (10)]. Studies of planar membranes [24–30] show that for the limiting and overlimiting current regimes, the solution is practically independent of the value of p for $p \gg 1$. For the spherical semiselective granule for the large enough external field E_∞ ($E_\infty > 5$) the solution of the problem does not depend on p (see Fig. 1).

The second BC in Eq. (10) means there is no flux of anions through the surface. The third condition sets a constant potential on the surface and, without loss of generality, this constant can be assumed to be zero. The last condition in Eq. (10) is the no-slip condition at the rigid surface.

At large distances away from the granule, the electrolyte solution becomes electroneutral, the electric field approaches the external applied field, and the fluid velocity approaches the electrophoretic velocity u_∞ , for $r \rightarrow \infty$,

$$c^+ \rightarrow 1, \quad c^- \rightarrow 1, \quad \frac{\partial \varphi}{\partial r} \rightarrow -E_\infty \cos \theta, \quad u \rightarrow -u_\infty \sin \theta, \quad v \rightarrow u_\infty \cos \theta. \quad (11)$$

The positive ions can penetrate the granule surface and their flux creates the electric current through the surface, for $r = 1$,

$$j = c^+ \frac{\partial \varphi}{\partial r} + \frac{\partial c^+}{\partial r}. \quad (12)$$

The cations do not accumulate inside the granule and the average density of the electric current must therefore be zero,

$$\int_0^\pi j \sin(\theta) d\theta = 0. \quad (13)$$

For a force-free particle, the viscous and the electrostatic forces are in balance,

$$\int_1^\infty \int_0^\pi \nabla(T_v + T_m) d\theta dr = 0, \quad (14)$$

where T_v and T_m are tensors of viscous and Maxwell-Wagner stresses.

Adding initial conditions for the cations and anions completes the system (4)–(14). These initial conditions arise from the following viewpoint: When there is no external electric field, the distribution of ions is homogeneous and neutral. This corresponds to the condition $c^+ = c^- = 1$. Some kind of perturbation should be superimposed on this distribution, to be natural from the viewpoint of the experiment (for $t = 0$),

$$c^+ = 1 + \hat{c}^+(r, \theta), \quad c^- = 1 + \hat{c}^-(r, \theta). \quad (15)$$

The so-called room perturbations that determine the external low-amplitude and broadband white noise should be imposed on the concentration. These perturbations are assumed to be exponentially decaying with r and are periodic with respect to the angle θ . The Fourier series with respect to θ was exploited: To mimic white noise, the amplitudes of the harmonics were taken to be equal to each other and equal to a certain small number and their phases were set by a random number generator with a uniform distribution in the interval $[0, \pi]$.

The nonlinear electrophoresis of ion-selective microparticles is described by a rather complicated set of coupled partial differential equations with singularities caused by a small parameter ν . Hence, the present problem is technically very challenging. In principle, the eventual purpose of our investigation is the evaluation of u_∞ . This requires the detailed calculation of all of the unknowns fields.

The problem is described by the four dimensionless parameters E_∞ , ν , \varkappa , and p . In this paper, we consider the case of large E_∞ and hence the solution is independent of p ; $p = 3$ is taken in all the calculations. We consider the electrolyte as a NaCl solution, thus \varkappa thus fixed, $\varkappa = 0.26$ (which corresponds to a NaCl solution with concentration $\tilde{c}_\infty = 0.1 \text{ mol/m}^3$). Hence, the solution of the problem for a fixed liquid and electrolyte depends on two parameters: the strength of the electric field E_∞ and the Debye number ν . In addition, it is known that for the plane membrane the dependence on ν for small ν is weak (see [25,27]). In all our calculations, ν is taken to be equal to 0.002 (which corresponds to the particle radius $\tilde{a} = 21.5 \text{ }\mu\text{m}$). Some calculations are performed for $\nu = 0.001$ to confirm a weak dependence for the case of microgranules.

III. RESULTS AND DISCUSSION

A. Qualitative structure of boundary layers

Our numerical analysis is accompanied by a semianalytical solution for the system (4)–(15). Such a combination of numerical and analytical solutions has allowed us to get a full description of electrophoresis in a wide range of experiments. Moreover, the semianalytical solution helps us understand the sophisticated structure of the electrostatic, concentration, and hydrodynamic fields near an ion-selective particle. It is convenient to introduce a new variable, counted from the interface, $y = r - 1$. In Fig. 3 the investigated region $0 < y < \infty$ and $0 < \theta < 180^\circ$ is divided into several subregions. Thin layers I–III are described by the inner solution, while the outer solution is related to region IV: I, the EDL region is located right next to the interface; II, the SCR of the thickness y_m is situated above the EDL; III, the diffusion layer of the thickness δ complements the boundary layers, nested inside each other; and IV, the electroneutral outer region with a constant conductivity $K = 2$. Note that we do not consider in our *ad hoc* model the jet of high conductivity,

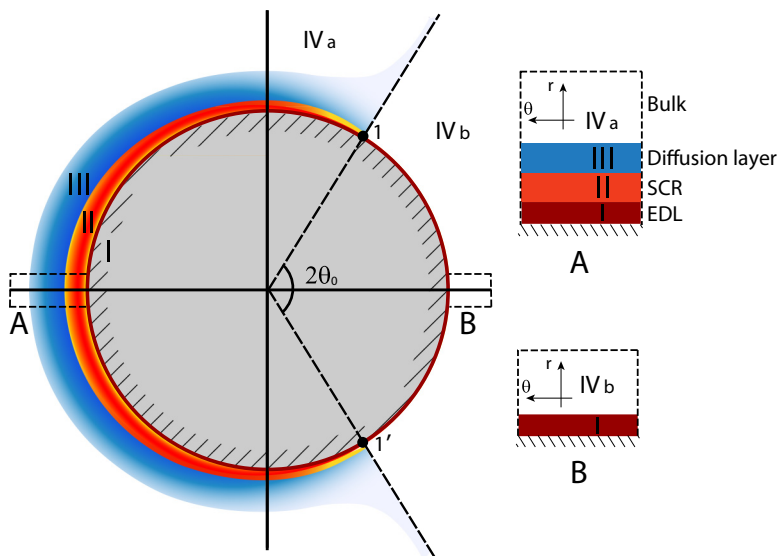


FIG. 3. Thin inner boundary layers, nested inside each other: the EDL, I; the SCR, II; and the diffusion layer, III. Also shown is the electroneutral outer region IV with $K = 2$. Points 1 and 1' separate regions of the incoming and outgoing fluxes. Inset A shows the typical structure of the incoming flux region. Inset B shows the typical structure of the outgoing flux region.

located behind the particle [see Fig. 6(a)], where salt advection becomes comparable to diffusion. A similar kind of far-field singularity was found for a highly charged colloidal particle (see [22]).

For the flat ion-selective membrane, the areas of the incoming and the outgoing ion fluxes are separated by the electrolyte layer (see, for example, Fig. 1 in Ref. [25]). An interesting peculiarity of the ion-selective particle is that the topology of the problem changes and both areas are located at the same interface, where the incoming and outgoing ion fluxes are separated by points 1 and 1', at which the electric current vanishes, $j(\theta_0) = 0$ (see Fig. 3). These points separate the EDL with a positive charge for the incoming current and the EDL with a negative charge for the outgoing current. The SCR exists only for the incoming flux region and disappears when approaching $\theta = \theta_0$. The electro-osmotic velocity generated at the boundary of the SCR creates a thin diffusion layer. At $\theta = \theta_0$ separation of the diffusion boundary layer is expected (see [37]).

Let us evaluate the lengths of the thin inner layers at $\nu \rightarrow 0$ and $E_\infty \rightarrow \infty$, leaving the question of the correlation between orders of ν and E_∞ open. The EDL length is $O(\nu)$, the evaluation of the SCR length y_m , taken from [24], yields $y_m = O(\nu^{2/3} E_\infty^{1/3})$, and it will be shown that the diffusion layer length is $O(E_\infty^{-1})$. Note that all three lengths are much smaller than the radius of the granule, the EDL length is much smaller than y_m [the last is satisfied if $E_\infty \leq O(\nu^{-2})$], and y_m/δ is $O(\nu^{2/3} E_\infty^{4/3})$, where δ is the diffusion length (see Fig. 3). We will further show that both layers have the same order of magnitude and the last ratio is $O(1)$.

B. Steady-state regime

The numerical method [27] for our work was generalized to the polar spherical coordinates. The time of establishment from the initial conditions (15) to the steady solution was in the interval $t_s = 0.1-1$. The results for the established solutions for $\varkappa = 0.26$ and $\nu = 0.002$ are presented below. Note that for $E_\infty < E_\infty^* \approx 27$, the imposed white noise disturbances decay and hence the steady-state solution is stable.

The total salt concentration $K(r, \theta) = c^+ + c^-$, also referred to as the electrical conductivity, is depicted in Figs. 4-6. In Fig. 4, the results for a moderate field $E_\infty = 5$ are presented. In the thin

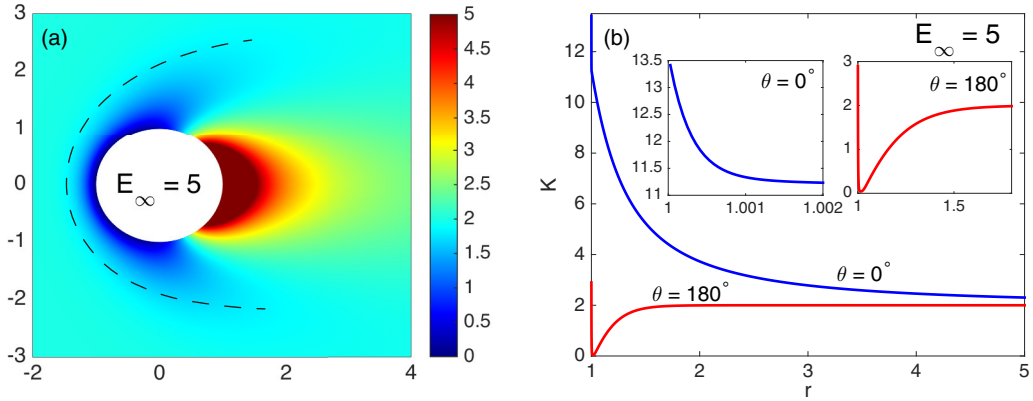


FIG. 4. (a) Electric conductivity $K(r, \theta)$ for a moderate external electric field $E_\infty = 5$. The dashed line stands for the edge of the diffusion layer. (b) Cross sections of $K(r)$ at $\theta = 0^\circ$ and $\theta = 180^\circ$. The behavior in the EDL, i.e., the depleted and enriched regions, is shown in the insets.

EDL, $K(r)$ exponentially decays; it varies more slowly outside the EDL. The influence of the EDL on the nonequilibrium phenomena is negligible and the role of the electric current is dominant. On the left-hand side of the granule, in the area of the incoming ion flux, with θ around 180° , there is a salt-depleted electroneutral region with small K as it takes place for flat membranes (see [23]). In this area, K changes from $K \approx 0$ near the microgranule to $K \approx 2$ at the edge of the diffusion boundary layer [as shown by the dashed line in Fig. 4(a)]. The diffusion layer increases downstream and eventually a separation of the diffusion layer takes place. This kind of separation was first described by Levich [37]; see also our semianalytical prediction presented in Sec. III D. On the right-hand side of the granule, in the area of the outgoing cations, with θ around zero, there is a salt-enriched region with large salt concentration K . Note that as the distance from the granule $y = r - 1$ increases, the salt concentration K tends to 2 on the right-hand side of the granule much slowly than on the left-hand side [see the insets in Fig. 4(b)]. As a result, two clouds of the salt concentration are formed: a cloud of the depleted electrolyte solution, elongated along the left-hand side of the microgranule, and a cloud of the enriched electrolyte solution, localized near the right-hand side of

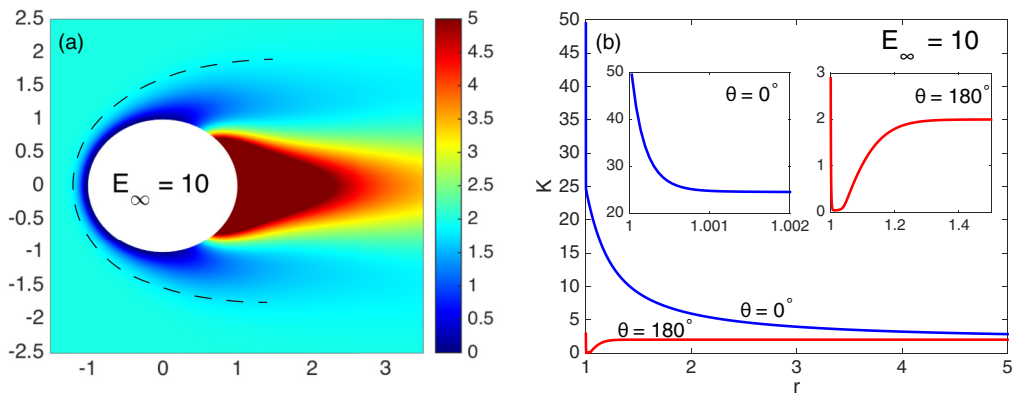


FIG. 5. (a) Electric conductivity $K(r, \theta)$ for $E_\infty = 10$. The dashed line stands for the edge of the diffusion layer. The values have been clipped from the actual maximal value down to $K = 5$ in order to achieve contrast with the diffusion layer. (b) Cross sections of $K(r)$ at $\theta = 0^\circ$ and $\theta = 180^\circ$. The behavior in the EDL, i.e., the depleted and enriched regions, is shown in the insets.

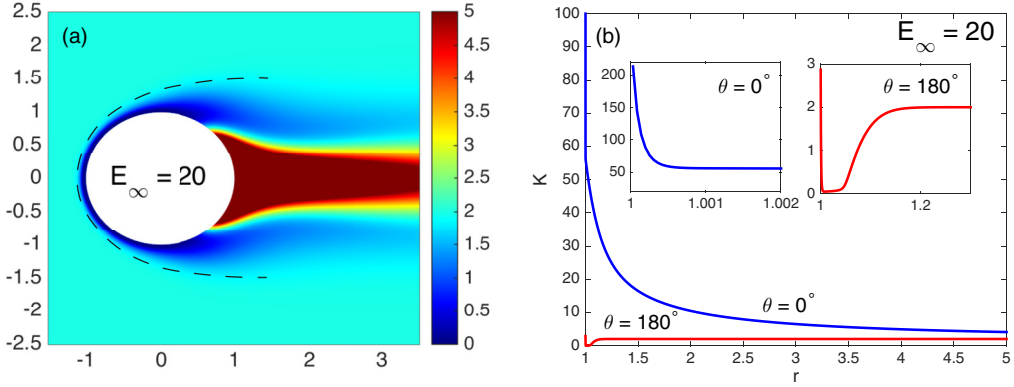


FIG. 6. (a) Electric conductivity $K(r, \theta)$ for $E_\infty = 20$. The dashed line stands for the edge of the diffusion layer. The values have been clipped from the actual maximal value down to $K = 5$ in order to achieve contrast with the diffusion layer. (b) Cross sections of $K(r)$ at $\theta = 0^\circ$ and $\theta = 180^\circ$. The behavior in the EDL, i.e., the depleted and enriched regions, is shown in the insets.

the granule. Far from these clouds, $K \rightarrow 2$. The decrease in the amount of electrolyte in the depleted region is compensated by its increase in the enriched region, so the total amount does not change,

$$\int_1^\infty \int_0^\pi (K - 2)r^2 d\theta dr = 0. \quad (16)$$

With an increase of the external field E_∞ , both electroneutral clouds of K change, but they do so in different ways. The thickness of the diffusion boundary layer at $\theta = 0^\circ$ in the depleted region decreases with an increase of E_∞ [compare the dashed lines in Figs. 4(a), 5(a), and 6(a)]. If the thickness of the diffusion layer at $\theta = 180^\circ$ for $E_\infty = 5$ is about 1.5, then for $E_\infty = 10$ it is about 1.2 and for $E_\infty = 20$ it is 1.1 [see the insets in Figs. 4(b), 5(b), and 6(b)]. The salt concentration in the electroneutral region on the right-hand side rapidly grows with increasing E_∞ . Moreover, the form of this region is strongly deformed and a cloudlike structure at $E_\infty = 5$ gradually transforms into an extended jetlike structure, where the salt is expelled off the granule at a larger speed.

The next important unknown is the charge density $\rho(r, \theta) = c^+ - c^-$; its distribution is illustrated in Figs. 7–9. At moderate fields $E_\infty = 5$, on the left-hand side of the microparticle, in the area of the incoming ion flux $\theta_0 < \theta < 180^\circ$, a positive electric charge is formed. Here θ_0

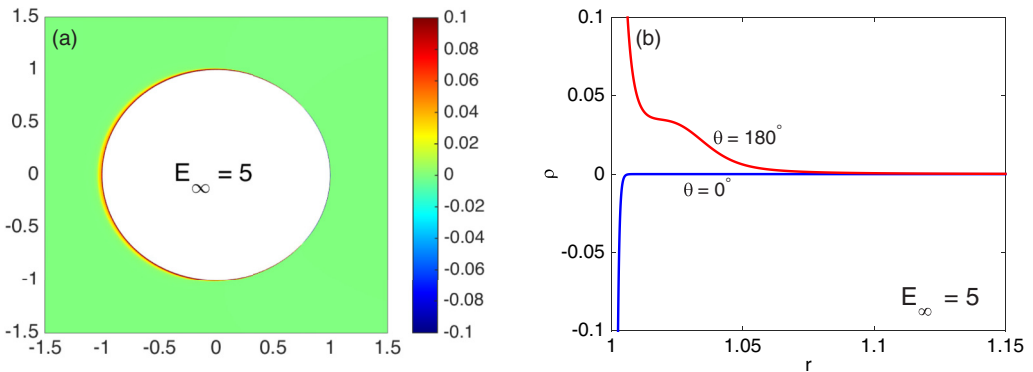


FIG. 7. (a) Charge density $\rho(r, \theta)$ for a moderate external electric field $E_\infty = 5$. (b) Cross sections of $\rho(r)$ at $\theta = 0^\circ$ and $\theta = 180^\circ$ near the granule surface.

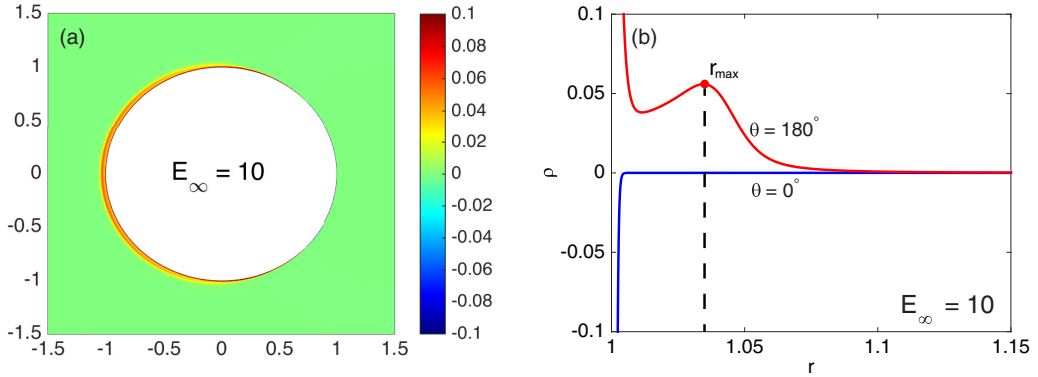


FIG. 8. (a) Charge density $\rho(r, \theta)$ for $E_\infty = 10$. (b) Cross sections of $\rho(r)$ at $\theta = 0^\circ$ and $\theta = 180^\circ$ near the granule surface.

corresponds to the limit of the SCR with $j = 0$ [see also Eq. (12)] and it is numerically estimated as $\theta_0 \approx 76^\circ$. For the moderate and large external field E_∞ , the nonequilibrium effects are dominant and $\rho(r, \theta)$ distribution is controlled by the ion flux through the granule. This consists of a thin EDL and the so-called space-charge region (SCR) with a characteristic local maximum away from the particle surface [see Fig. 7(b)]. The formation of the SCR for the limiting currents is a well-known nonequilibrium phenomenon and was first described for flat membranes by Rubinstein and Shtilman [23] (see also [25,26]). Note that the total charge in the SCR is much larger than in the EDL. The SCR coincides in the space with the depleted region for the salt concentration. Far from the interface, $\rho \rightarrow 0$ and the solution becomes electroneutral. On the right-hand side of the microparticle, in the area of the outgoing ion flux $0 < \theta < \theta_0$, a negative electric charge is formed. The SCR is absent in this area and it contains only a thin quasiequilibrium EDL; ρ exponentially decays with increasing of $r - 1$ [see Fig. 7(b)]. With an increase of the external field E_∞ , the total charge in the SCR grows, the point of maximal ρ , $r_{\max} = y_m + 1$, departs further from the surface of the granule, the area of the incoming ion flux is extended, and the area of the outgoing flux shrinks: For $E_\infty = 5$, $\theta_0 \approx 76^\circ$, while for $E_\infty = 20$, $\theta_0 \approx 59^\circ$.

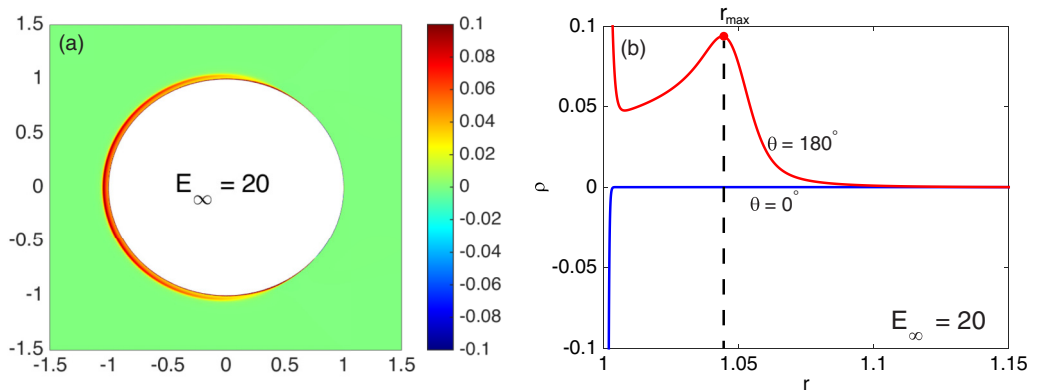


FIG. 9. (a) Charge density $\rho(r, \theta)$ for $E_\infty = 20$. (b) Cross sections of $\rho(r)$ at $\theta = 0^\circ$ and $\theta = 180^\circ$ near the granule surface.

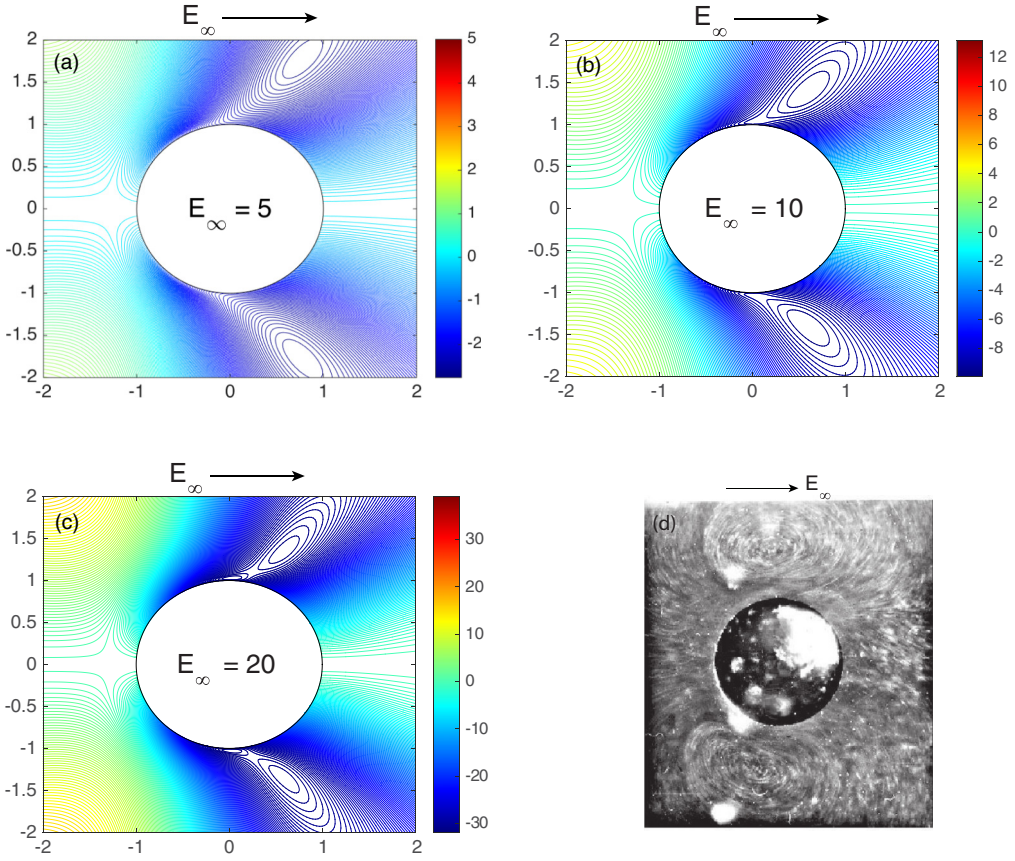


FIG. 10. Theoretical stream function distribution for (a) $E_\infty = 5$, (b) $E_\infty = 10$, and (c) $E_\infty = 20$. (d) Electrokinetic flow from [38] around a 1-mm ion-selective particle at $\tilde{E}_\infty = 100$ V/cm, which corresponds to dimensionless $E_\infty = 200$ and Debye number $\nu \approx 8.68 \times 10^{-5}$.

The stream function for the axisymmetric case $\psi(r, \theta)$ in the polar spherical coordinates is defined as

$$u = -\frac{1}{\sin \theta} \frac{1}{r} \frac{\partial \psi}{\partial r}, \quad v = \frac{1}{\sin \theta} \frac{1}{r^2} \frac{\partial \psi}{\partial \theta}.$$

The distribution of the stream function $\psi(r, \theta)$ for $E_\infty = 5$, 10, and 20 is illustrated in Fig. 10(a)–10(c), respectively. An interesting phenomenon can be noticed: Large vortices form on the right hand-side of the particle. These vortices were experimentally discovered by Dukhin *et al.* [38] and are called Dukhin-Mishchuk vortices. They are generated at sufficiently large strength of the external electric field. The physical reason for their appearance is rather simple: The positive electric charge in the SCR, in combination with the tangential component of the electric field to the granule surface, produces the Coulomb force, which in turn creates the electro-osmotic velocity near the particle. Our numerical simulation results in Figs. 10(a)–10(c) show good qualitative agreement with regard to the appearance of Dukhin vortices.

When the boundary is curved and the applied field is sufficiently strong, a similar transition may occur over part of the boundary. This renders a more complex electrokinetic flow mechanism, termed electro-osmosis of the second kind [7]. Dukhin in Ref. [7] suggested that the familiar Smoluchowski slip formula could be applied to second-kind electro-osmosis in overlimiting conditions, provided the ζ potential also accounts for the voltage drop on the space-charge layer.

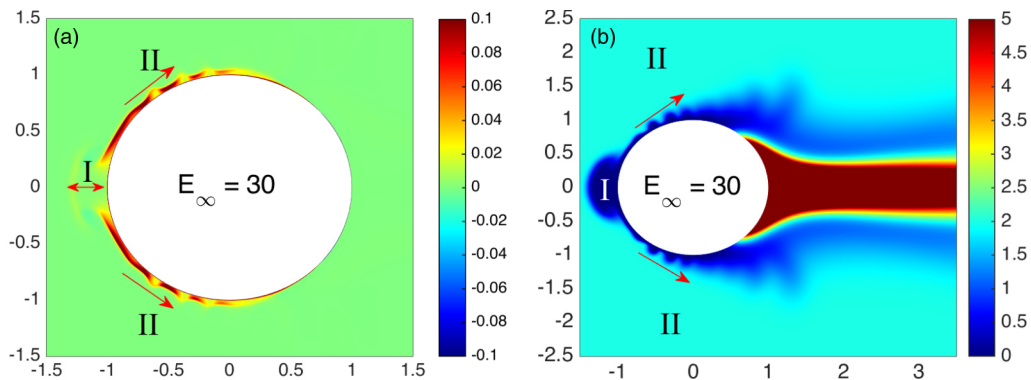


FIG. 11. (a) Charge distribution $\rho = c^+ - c^-$ and (b) electric conductivity $K = c^+ + c^-$, with $E_\infty = 30$ for regions I and II of the standing and traveling waves, respectively. Arrows show the direction of propagation.

Using these heuristic arguments, Dukhin obtained [7] an electrophoretic velocity that scales as the square of the applied field. This analysis was improved by Mishchuk and Takhistov [31]. Ben *et al.* employed asymptotic methods to derive an approximate current-voltage characteristics for a one-dimensional model problem. Using these characteristics to describe the transport process on the cathodic hemisphere, the authors obtained a more sophisticated model for the electrophoretic problem. In a later analysis, Ben *et al.* [39] found a different scaling for the velocity, as the electric field to the $2/3$ power, at the large-Péclet-number limit. Both of these power-law predictions are in some qualitative agreement with existing experimental data for different regimes (see [7,40]). A different velocity scaling, with the third power of the electric field, was found by Zaltzman and Rubinstein [25] (see also [41]).

The tangential component of the velocity is diminished (the liquid flow slows down) and the normal component of the velocity field increases due to the mass conservation [Eq. (9)]. The consequences of this increase and decrease of the components of the velocity field lead to a vortex.

C. Electrokinetic instability and transition to the chaotic regime

At the external electric field above the critical one (steady to unsteady), $E_\infty > E_\infty^*$ and $E_\infty^* \approx 27$ (estimated from numerical simulations), the imposed white-noise disturbances (15) grow and finally destroy the steady-state solution. The previously described steady-state regime loses its stability with respect to the electrokinetic mode. The electrokinetic instability of a one-dimensional quiescent state in flat membranes was discovered by Rubinstein and Zaltzman [24,25]; for the cation-exchange membranes this instability occurs near the surface of the incoming ion flux. Near the outgoing-ion-flux surface, the solution is stable.

Three factors make the present case of the electrokinetic instability more complicated and more peculiar than the case of a flat membrane: (i) the steady state is not a one-dimensional solution, (ii) convection of salt and liquid occurs, and (iii) both surfaces of the incoming and outgoing fluxes are geometrically just two fragments of the entire granule surface and there is a singularity at their junction at $\theta = \theta_0$ (see the semianalytical solution in the following section).

The instability is possible only on the left-hand side of the particle, in the SCR and the diffusion boundary layer. Indeed, our numerical solution shows that for a small supercriticality $E_\infty > E_\infty^*$, in a small vicinity of $\theta = 180^\circ$, the flow becomes unstable and small sinusoidal waves propagate along the granule's surface towards smaller angles θ and finally decay at $\theta = \theta_0$. The flow on the right-hand side of the microparticle is always stable.

Figure 11 shows snapshots for the charge density ρ and the salt concentration K far from the threshold of instability for the strongly nonlinear regime, $E_\infty = 30$. Periodic oscillations of the charge density and the salt concentration occur in region I. These oscillations are perpendicular

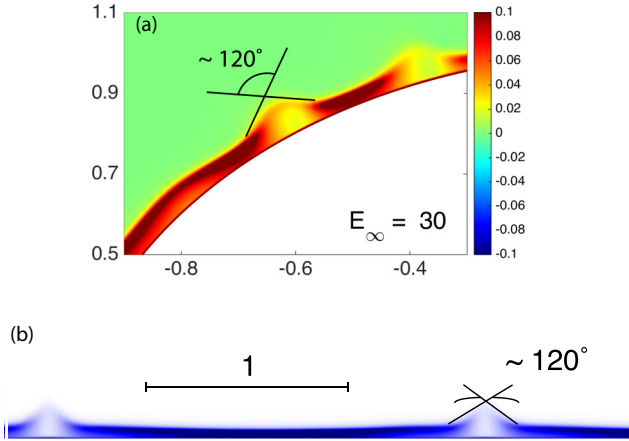


FIG. 12. (a) Blow-up of region I of Fig. 11(a). (b) Spikes for a flat membrane [27,42]. The normal to the membrane coordinate is strongly compressed in comparison to the direction along the membrane.

to the microgranule's surface and they are rather strong. They completely destroy the classical texture of the SCR, the depleted region, and the diffusion layer, but the EDL is not affected by these oscillations. They can be interpreted as strongly nonlinear standing waves. At the sides of region I, in region II, these standing waves cause nonlinear traveling waves. Figure 11(a) shows that propagating disturbances of the charge density ρ take a spiked shape, as it was first described in the works [26–28,42] on flat membranes. There is a rather sharp boundary between the space-charge region and the diffusion region. The salt concentration K of the traveling waves forms cloudlike structures. See the Supplemental Material in [43] for video of these instabilities from our direct numerical simulation (DNS) for $\rho(r, \theta, t)$ and $K(r, \theta, t)$.

In Fig. 12, a small vicinity of region II from Fig. 11(a) is compared with the distribution of ρ calculated numerically for a flat membrane (see [27,42]). There is a striking similarity between the distributions: Inside the spikes, ρ is very small (the spikes are “empty”). The spikelike structures are joined by thin regions of large space charge. The work by Shelistov *et al.* [44] has shown that the opening angle of the spike does not depend on the parameters of the problem and is about $\theta_s \approx 120^\circ$. This evaluation is applicable not only for flat membranes, but also for a more complicated case of a corrugated membrane (see [45] and Fig. 4). In the present case, the spikelike coherent structures are not quiescent: They propagate towards smaller angles and hence they should be disturbed by the convection. Still, θ_s is close to 120° ; this angle did not change in our other calculations with different E_∞ .

In region I of Fig. 11, all the unknowns vary periodically with time, forming a standing wave near the pole. The charge density ρ and the salt concentration K at $\theta = 180^\circ$ as a function of the radius r for different time instants are shown in Fig. 13. Without loss of generality, the initial time can be assumed to be zero, $t = 0$.

At $t = 0$, the large-amplitude space charge is located close to the interface $r = 1$ and it moves towards the larger r . At $t = 0.005$, the charge is spread in space, it is located far from the interface, and its amplitude is significantly reduced. At $t = 0.03$, the small-amplitude charge turns back, and at $t = 0.075$ it returns to the same position and restores its profile and value. This time is in fact a period; the process is repeated periodically.

At $t = 0$, the salt concentration has a small flat depleted region with $K \approx 0$ and a flat region of electroneutral solution with $K = 2$, which are connected by a kink, together forming a frontal concentration wave. The front concentration wave moves away from the granule surface, towards larger r , and the depleted region is expanding. The concentration in the EDL is unaffected during the process. These kinds of concentration waves, called shock waves, were found by Bazant [14].

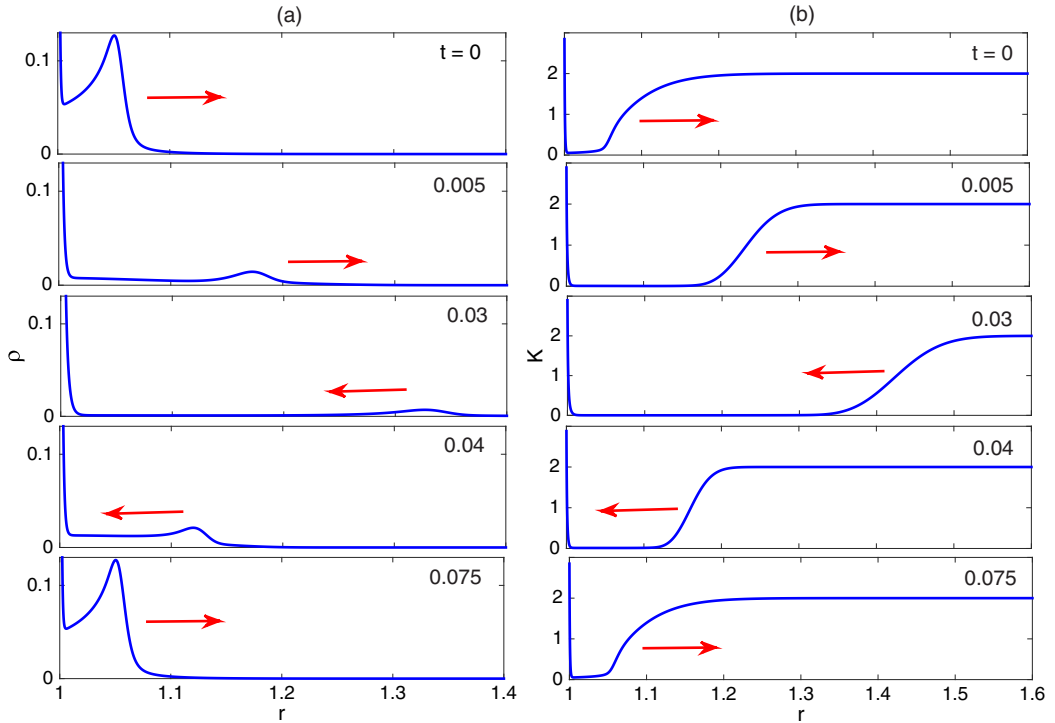


FIG. 13. (a) Cross section of $\rho(r)$ at $\theta = 180^\circ$ and at different time instants. (b) Cross section of $K(r)$ at $\theta = 180^\circ$ and at different time instants. The wave is bouncing back from the edge of the diffusion layer defined by δ .

At $t = 0.03$, the shock wave comes back and eventually returns to the same position and restores its profile and value. This process is repeated periodically. If the radius of the granule varies from 25 to 250 μm , for the aqueous solution of NaCl, dimensional period varies from 0.05 to 5 s (the corresponding typical frequency of oscillation is within the window from $\tilde{f} = 20$ Hz to $\tilde{f} = 0.2$ Hz).

The description of the hydrodynamic fields completes the picture. A snapshot of the unstable regime is shown in Fig. 14. The standing wave at $\theta = 180^\circ$ creates the Rubinstein-Zaltzman microvortices I, which are convected towards the smaller angles. As for a flat membrane [26,42], these microvortices are located in a thin diffusion layer. Upon reaching the angle $\theta = \theta_0$, the Rubinstein-Zaltzman microvortices eventually merge with the Dukhin-Mishchuk vortices II and completely disappear. The microvortices I cannot penetrate the Dukhin-Mishchuk vortices II and the region of the outgoing ion flux $0 < \theta < \theta_0$ is completely quiescent. See the Supplemental Material in [43] for videos of DNS for the stream function for different E_∞ .

The electric current that is created by the flux of cations on the surface, j , normalized by its maximum value j_{max} , as a function of the angle θ , is shown in Fig. 15 for different values of E_∞ . The area of the incoming ion flux for $E_\infty = 30$ is approximately two times larger than the area of the outgoing flux $\theta_0 \approx 63^\circ$, which represents the separation angle of the regions of incoming and outgoing ion fluxes. The maximal absolute value of the current in the area of outgoing ion flux is three to five times larger than that in the incoming area. The depicted profile for the electric field leading to an unstable regime $E_\infty = 30$ is a snapshot and the solid line stands for some time instant $t = t_0$. The oscillations connected with the electrokinetic instability are clearly seen in the snapshot; the instability starts at $\theta = 180^\circ$ and ends at $\theta = \theta_0$. The dashed line stands for the electric current at the next time instant $t = t_0 + \Delta t$, $\Delta t = 0.0008$. The velocity of the propagating wave can be evaluated as $c_v \approx 250$.

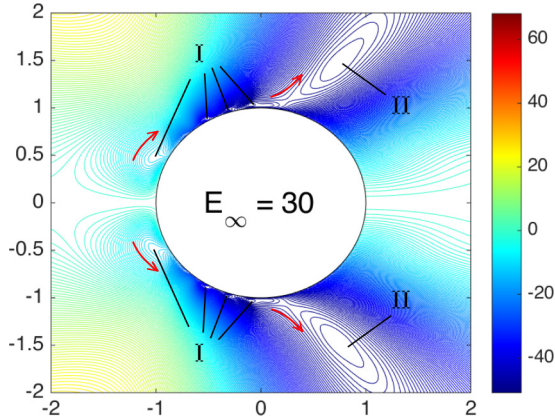


FIG. 14. Stream-function distribution for the unstable regime $E_\infty = 30$. Here I stands for the Rubinstein-Zaltzman microvortices and II stands for the Dukhin-Mishchuk vortices. The arrows show the propagation of the Rubinstein-Zaltzman microvortices.

The nonlinear electrophoretic velocity u_∞ is plotted as a function of E_∞ in Fig. 16. At $E_\infty = 10$, at a sufficiently large time, the steady-state solution is established and u_∞ does not change with time, $u_\infty = 18.72$. At a small supercriticality $E_\infty = 27$, the established electrophoretic velocity u_∞ is not constant, but sinusoidally varies with time, so the average velocity is $\langle u_\infty \rangle = 94.9$ and the amplitude of oscillations $\Delta u_{\max} = 0.06$. With an increase of E_∞ to 28, the oscillations

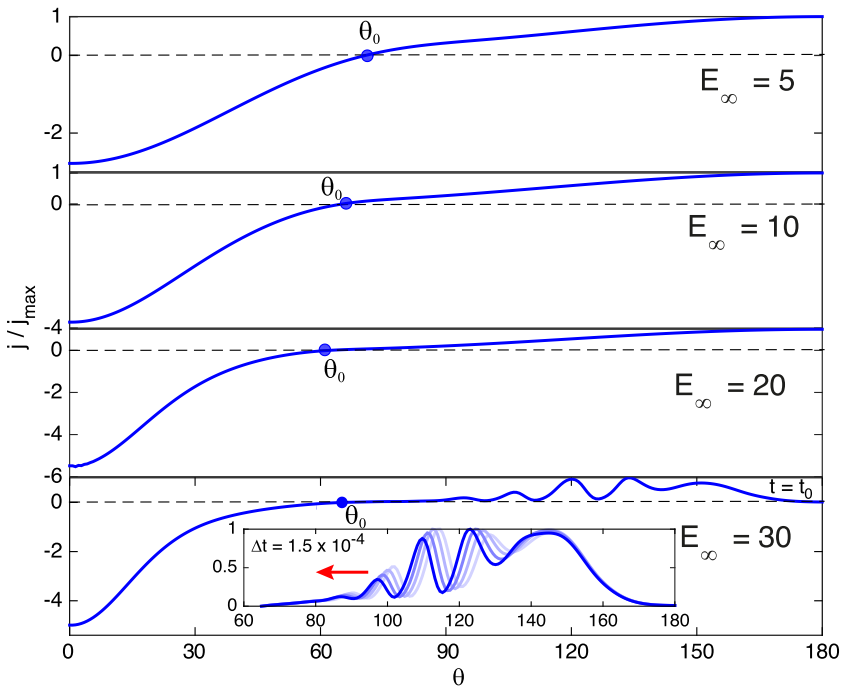


FIG. 15. Electric current normalized to its maximum value along the microgranule surface $0 < \theta < 180^\circ$, for different strengths of the external field E_∞ . The inset shows the variation of the ion flux in time for the unstable case, which shows a traveling wave. In this inset, all subsequent curves are for $t_0 + n\Delta t$, $n = 1, 2, 3$.

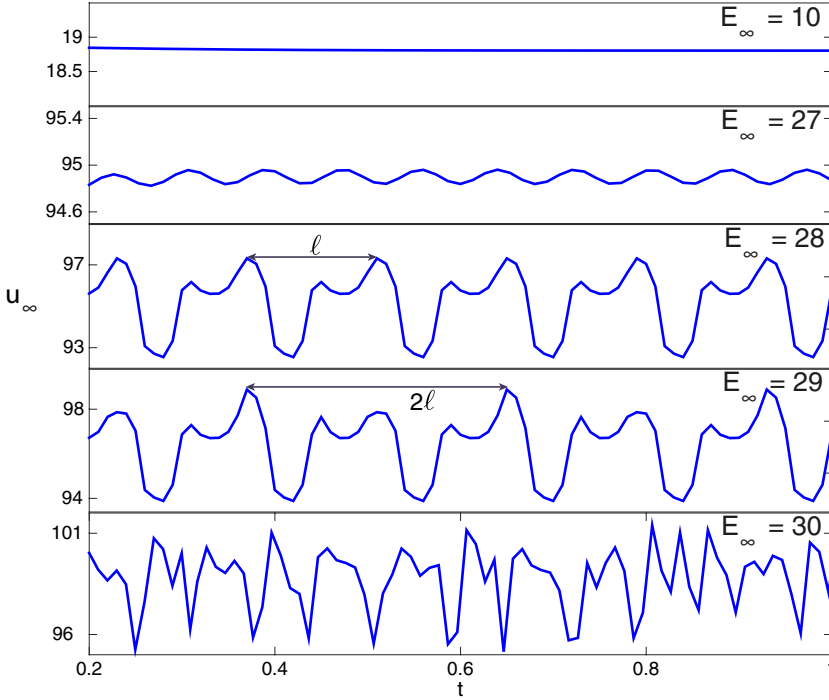


FIG. 16. Time records of the electrophoretic velocity u_∞ at different strengths of the electric field E_∞ .

lose their sinusoidal nature but remain periodic. With a further increase of E_∞ , period-doubling bifurcation or the subharmonic transition, $E_\infty = 29$, occurs. Soon after the first period doubling, the regular oscillations are replaced by the chaotic ones, $E_\infty = 30$. It is reasonable to assume that the Feigenbaum scenario [46,47] is responsible for this transition. Note that, because of high viscosity, the oscillations of u_∞ , either periodic or chaotic, have a small amplitude, not more than 5%–6% of the mean velocity, and hence it is difficult to detect them in experiment.

D. Semianalytical solution of the problem at $E_\infty \rightarrow \infty$ and $\nu \rightarrow 0$

1. The EDL (region I) and SCR (region II)

In the thin EDL and the SCR $\partial/\partial t, \partial/\partial \theta \ll \partial/\partial y$, with $y = r - 1$, and the solution can be assumed locally steady and one dimensional and hence Eqs. (4)–(6) transform into one nonlinear ordinary differential equation (ODE) (see [24,25])

$$\nu^2 \frac{d^2 E}{dy^2} + \left[j(y_m - y) - \frac{\nu^2}{2} E^2 \right] E + j = 0, \quad (17)$$

where $E \equiv \partial\varphi/\partial y$ and y_m is an unknown constant of integration. The influence of the EDL for the extreme overlimiting regimes is negligible [24], and in the present formulation it will be neglected. Note that generalizing the basic ideas of [25] for the present problem and taking into account the influence of the EDL would allow us to develop a semianalytical approach, encompassing all regimes from the quasiequilibrium one to the extreme nonequilibrium one. However, this approach requires inadmissibly cumbersome calculations and formulas. For extreme nonequilibrium conditions, as $\nu \rightarrow 0$ and $E > O(\log_{10} \nu)$, the ODE (17) becomes a cubic algebraic equation

$$\left[j(y_m - y) - \frac{\nu^2}{2} E^2 \right] E = 0. \quad (18)$$

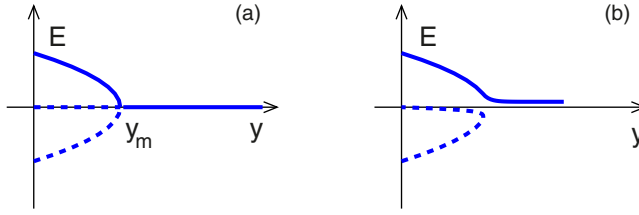


FIG. 17. Schematic bifurcation diagrams. (a) Solutions of Eq. (18) have an imperfect pitchfork bifurcation, which is structurally unstable [48]. (b) Plot of Eq. (17); for a small but finite v this kind of bifurcation is destroyed. The solid line corresponds to the solution that makes physical sense.

Equation (18) has three solutions (see Fig. 17), but only two of them make physical sense. The first one is valid in the SCR,

$$E = \frac{1}{v} \sqrt{2j(y_m - y)}, \quad v\varphi = \frac{2\sqrt{2}}{3j} (jy_m)^{3/2} - \frac{(2jy_m - 2jy)^{3/2}}{3j} \quad \text{for } 0 < y < y_m. \quad (19)$$

The relations (19) make sense only inside the region $0 < y < y_m(\theta)$ and the constant of integration y_m acquires the physical meaning of the SCR length. The dependence on the angle θ is parametric. Let us designate $\Delta\varphi$ as a potential drop across the SCR, $0 < y < y_m$; then from the second relation of (19) it follows that

$$v\Delta\varphi = \frac{2\sqrt{2}}{3} y_m^{3/2} j^{1/2}. \quad (20)$$

The relation (20) can be rewritten in the convenient form

$$y_m^3 = \frac{9}{8} v^2 \frac{\Delta\varphi^2}{j}. \quad (21)$$

The SCR coincides with the salt-depleted region; in the approximation adopted, for $0 < y < y_m$, the salt concentration $K = 0$.

Since the independent variables of the system in the SCR are not constant with respect to the angle but instead are slowly varying functions, $\partial/\partial\theta \ll \partial/\partial y$ gives rise to nonzero electro-osmotic velocity components $v \ll u$. Equations (7) and (8) in the SCR are transformed into

$$-\frac{\partial\Pi}{\partial X} = \frac{\partial^2 u}{\partial y^2} - \varkappa \frac{\partial E}{\partial y} \frac{\partial\varphi}{\partial X}, \quad \frac{\partial\Pi}{\partial y} = \varkappa E \frac{\partial E}{\partial y}, \quad (22)$$

with the boundary conditions

$$\begin{aligned} u &= 0 \quad \text{for } y = 0, \\ \frac{\partial u}{\partial y} &= 0 \quad \text{for } y = y_m, \end{aligned} \quad (23)$$

where $X \equiv \pi - \theta$. The solution of (22) and (23) results in the electro-osmotic slip velocity $u_m = u(y_m)$ (see [24]),

$$\frac{1}{\varkappa} u_m = \frac{1}{8} \Delta\varphi^2 \frac{1}{j} \frac{\partial j}{\partial X} + \frac{1}{2} \frac{\partial}{\partial X} \Delta\varphi^2. \quad (24)$$

The normal velocity component at y_m , v_m , can be neglected for a flat membrane, but for the spherical granule it becomes important in the diffusion layer and should be taken into account. This component can be found from the mass balance equation (9) as

$$v_m + u_m \frac{\partial y_m}{\partial X} = \frac{\varkappa}{v^2} \frac{1}{\sin X} \frac{\partial}{\partial X} \left[\sin X \left(\frac{7}{20} y_m^4 \frac{\partial j}{\partial X} + \frac{4}{5} y_m^3 j \frac{\partial y_m}{\partial X} \right) \right]. \quad (25)$$

The electro-osmotic velocity in the region of the outgoing ion flux for the extreme overlimiting regimes is negligibly small, $u_m = v_m = 0$.

2. Self-similar solution for the diffusion boundary layer (region III)

The thin electroneutral diffusion layer is located above the SCR, $y > y_m$, and it has a characteristic length $\delta(X)$. In this layer, the salt concentration K is convected along the granule surface at the electro-osmotic velocity and at the same time diffuses from $K = 0$ in the depleted region to the equilibrium value $K = 2$ in the outer bulk region. By adding Eqs. (4) and (5) and assuming that the diffusion layer thickness δ is small in comparison with the granule radius, we obtain the convection-diffusion equation in the boundary-layer approximation

$$\frac{\partial K}{\partial t} + U \frac{\partial K}{\partial \theta} + V \frac{\partial K}{\partial y} = \frac{\partial^2 K}{\partial y^2}. \quad (26)$$

At $y = y_m$, at the boundary of the depleted region, the salt concentration is assumed to be zero and its flow normal to the surface; the ion flux is determined by diffusion, as

$$K = 0, \quad \frac{\partial K}{\partial y} = j \quad \text{for } y = y_m. \quad (27)$$

At the outer edge of the diffusion layer, the salt concentration tends to the equilibrium value

$$K = 2 \quad \text{for } y - y_m \gg \delta. \quad (28)$$

In a thin diffusion layer, the tangential velocity can be assumed to be constant with respect to y and equal to the electro-osmotic slip velocity $u = u_m(X)$, but it varies along the surface. To find the normal velocity v , we will use the mass balance equation (6),

$$\frac{\partial}{\partial y}(v \sin \theta) + \frac{\partial}{\partial \theta}(u \sin \theta) = 0. \quad (29)$$

Upon changing the independent variable $X = \pi - \theta$ and integrating (29), we get

$$\int_{y_m(X,t)}^y \frac{\partial}{\partial y}(v \sin X) dy - \int_{y_m(X,t)}^y \frac{\partial}{\partial X}(u \sin X) dy = 0, \quad (30)$$

from which the relation for v follows,

$$v \sin X = v_m \sin X + \eta \frac{\partial}{\partial X}(u_m \sin X), \quad (31)$$

where $\eta \equiv y - y_m$ and the v component is formed by the electro-osmotic portion v_m (in fact, it is a liquid suction from the SCR) and by the variation of the longitudinal component u_m along the granule. Equation (26), upon substitution of (31), becomes a linear partial differential equation (PDE) with respect to K ,

$$\frac{\partial K}{\partial t} \sin X - u_m \sin X \frac{\partial K}{\partial X} + \eta \frac{\partial}{\partial X}(u_m \sin X) \frac{\partial K}{\partial \eta} + W_m \sin X \frac{\partial K}{\partial \eta} = \frac{\partial^2 K}{\partial \eta^2} \sin X, \quad (32)$$

where u_m and v_m are determined by relations (24) and (25) and

$$W_m \equiv -\frac{\partial y_m}{\partial t} + \left(v_m + \frac{\partial y_m}{\partial X} u_m \right),$$

with the BCs

$$\begin{aligned} K &= 0, \quad \frac{\partial K}{\partial \eta} = j \quad \text{for } \eta = 0, \\ K &= 2 \quad \text{for } \eta/\delta \rightarrow \infty. \end{aligned} \quad (33)$$

The necessity of solving (32) and (33) even for a steady case $\partial/\partial t = 0$ would greatly complicate our model if the problem did not have an analytical self-similar solution. Indeed, let us seek a solution of Eq. (32) in the self-similar form

$$K = K(Y) \quad \text{where } Y = \frac{\eta - b(X, t)}{\delta(X, t)}, \quad \frac{d^2 K}{dY^2} + 2Y \frac{dK}{dY} = 0, \quad (34)$$

where $b(X, t)$ is an arbitrary self-similar function. Upon substitution of (34) into (32) and separation of the b terms and δ terms, we get two one-dimensional PDEs

$$\frac{\partial \delta}{\partial t} \sin X - \frac{\partial}{\partial X}(u_m \delta \sin X) = \frac{2}{\delta} \sin X, \quad (35)$$

$$\frac{\partial b}{\partial t} \sin X - \frac{\partial}{\partial X}(u_m b \sin X) = W_m \sin X. \quad (36)$$

The third equation, the algebraic one, can be derived from the solution of ODE (34), $K = \text{const}_1 \text{erf}(Y) + \text{const}_2$, by substituting the BC (33) into it,

$$j\delta = \frac{4}{\sqrt{\pi}} \frac{\exp(-b^2/\delta^2)}{1 - \text{erf}(-b/\delta)}. \quad (37)$$

Let us stretch the unknowns so that in the new form they are $O(1)$,

$$\begin{aligned} u_m &= E_\infty^2 U_m, & v_m &= E_\infty^2 V_m, & \psi &= E_\infty^2 \Psi, & u_\infty &= E_\infty^2 U_\infty, \\ \Delta \varphi &= E_\infty F, & \varphi &= E_\infty \Phi, & j &= E_\infty J, & \partial/\partial t &= E_\infty^2 \partial/\partial T, \\ b &= v^{2/3} E_\infty^{1/3} B, & y_m &= v^{2/3} E_\infty^{1/3} Y_m, & \delta &= E_\infty^{-1} \Delta. \end{aligned} \quad (38)$$

The system (35)–(37) after substitution of the relations (24) and (25) for u_m and v_m turns into the system

$$\frac{\partial \Delta}{\partial T} \sin X - \varkappa \frac{\partial}{\partial X} \left(\frac{F^2 \Delta}{8J} \frac{\partial J}{\partial X} + \frac{\Delta}{2} \frac{\partial F^2}{\partial X} \right) = \frac{2}{\Delta} \sin X, \quad (39)$$

$$\begin{aligned} \frac{\partial B}{\partial T} \sin X - \varkappa \frac{\partial}{\partial X} \left[\left(\frac{F^2}{8J} \frac{\partial J}{\partial X} + \frac{1}{2} \frac{\partial F^2}{\partial X} \right) B \sin X \right] \\ = \varkappa \frac{3^{8/3}}{16} \frac{\partial}{\partial X} \left\{ \left[\frac{7}{20} \frac{F^{8/3}}{J^{4/3}} \frac{\partial J}{\partial X} + \frac{J}{5} \frac{\partial}{\partial X} \left(\frac{F^{8/3}}{J^{4/3}} \right) \right] \sin X \right\} - \frac{3^{2/3}}{2} \sin X \frac{\partial}{\partial T} \left(\frac{F^{2/3}}{J^{1/3}} \right), \end{aligned} \quad (40)$$

$$J\Delta = \frac{4}{\sqrt{\pi}} \frac{\exp(-\chi^2 B^2/\Delta^2)}{1 - \text{erf}(-\chi B/\Delta)}, \quad (41)$$

with respect to four unknown functions J , F , Δ , and B . The BCs for the unknowns are conditions of symmetry at the pole,

$$\frac{\partial \Delta}{\partial X} = 0, \quad \frac{\partial F}{\partial X} = 0, \quad \frac{\partial J}{\partial X} = 0, \quad \frac{\partial B}{\partial X} = 0 \quad \text{at } X = 0. \quad (42)$$

At $X \rightarrow X_0$, which corresponds to $\theta \rightarrow \theta_0$, the electric current $J \rightarrow 0$ by definition. After a brief analysis of Eq. (41) it can be shown that $\Delta \rightarrow \infty$ at $X \rightarrow X_0$, because the right-hand side of Eq. (41) is always positive. We conclude that the left-hand side could not tend to zero at $X \rightarrow X_0$, so Δ has to tend to infinity, which in turn indicates the separation of the diffusion boundary layer. This kind of separation was originally predicted by Levich [37] and can be seen in Figs. 5(a) and 6(a) resulting from the DNS, so the theoretical foundations are now clearly shown for this problem of separation.

TABLE I. Typical values of parameters.

\tilde{a} (μm)	E_∞	ν	χ
25	10	4×10^{-4}	0.117
25	1000	4×10^{-4}	54.3
500	10	2×10^{-5}	0.0159
500	1000	2×10^{-5}	7.368

The two small parameters of the system ν and E_∞^{-1} are now absorbed into one parameter $\chi = O(1)$,

$$\chi = \nu^{2/3} E_\infty^{4/3} = \frac{O(y_m)}{O(\delta)}.$$

Note that χ is the ratio of the SCR characteristic length $\nu^{2/3} E_\infty^{1/3}$ and the characteristic diffusion length E_∞^{-1} [see the stretching parameters in Eq. (38)]. This ratio χ is evaluated in Table I with $\tilde{\lambda}_D = 10$ nm, $\tilde{a} = 25$ μm to 500 nm, and $E_\infty = 10$ – 10^3 .

In order to close the analytical solution of the whole problem, we need to find a solution in the outer bulk region. This solution has been developed in Ref. [49] and is given in the Appendix.

3. Results for the steady-state case, linear stability, and comparison with the DNS results

For the steady-state solution ($\partial/\partial T = 0$), Eqs. (39)–(41) and (A6) become a system of three first-order ODEs and one singular integral equation. Boundary conditions (42) make the system complete. The finite-difference method with uniform grid $\theta^{(1)}, \theta^{(2)}, \dots, \theta^{(n)}$ (or $X^{(1)}, X^{(2)}, \dots, X^{(n)}$) with respect to the angle transforms this system into a system of nonlinear algebraic equations with respect to the unknowns $J^{(k)}, F^{(k)}, \Delta^{(k)}$, and $B^{(k)}$ in the mentioned grid points. This system was solved by Newtonian method and the results are comparable to those obtained by the DNS [27].

At $\chi = \chi_*$, the one-dimensional steady-state solution (19) becomes unstable with respect to small time perturbations

$$\begin{aligned} \Delta &= \Delta_0(r, \theta) + \hat{\Delta}(r, \theta) \exp(i\lambda T), & J &= J_0(r, \theta) + \hat{J}(r, \theta) \exp(i\lambda T), \\ B &= B_0(r, \theta) + \hat{B}(r, \theta) \exp(i\lambda T), & F &= F_0(r, \theta) + \hat{F}(r, \theta) \exp(i\lambda T). \end{aligned} \quad (43)$$

These relations were substituted into the finite-difference analog of Eqs. (39)–(42) and (A6) and linearized. The resulting generalized algebraic eigenvalue problem was solved by the QR algorithm [50].

It can be readily seen from (39)–(41) that at $X \rightarrow X_0$ (or at $\theta \rightarrow \theta_0$) the SCR length tends to zero but the diffusion boundary layer $\Delta \rightarrow \infty$. The last phenomenon is called separation of the diffusion boundary layer (see [37]). Such a separation can be clearly seen from our DNS for the steady regimes [see Fig. 6(a)] and even for the nonsteady regimes [see Fig. 11(b)]. An important characteristic, the point of separation θ_0 , obtained by the semianalytical approach and by the DNS, is presented in Fig. 18. Note that for $\chi > 1.28$, the steady-state solution of the semianalytical statement is compared with the unsteady solution of the DNS. As we mentioned earlier, the oscillations of the unknowns, for either periodic or chaotic regimes, have a small amplitude that is not more than 6% of the mean value. In Fig. 18, the averaged values of $\langle \theta_0 \rangle = 1/(t_2 - t_1) \int_{t_1}^{t_2} \theta_0 dt$ are given for the DNS results for a sufficiently long interval of averaging. There is fairly good agreement between analytical and numerical approaches, except for $\chi < 1.28$. For $\chi < 1.28$, DNS results go far beyond the analytical results because they belong to the regime of underlimiting currents (for fixed ν and for small values of χ , E_∞ will be small, which contradicts the hypothesis of analytical considerations, $E_\infty \rightarrow \infty$).

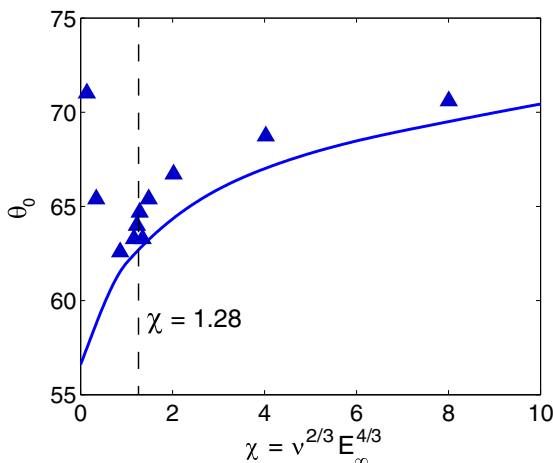


FIG. 18. Separation angle of the diffusion boundary layer θ_0 versus χ at $\varkappa = 0.26$. The solid line stands for the semianalytical solution and the triangles stand for the numerics.

The potential distribution [represented by the stretched variable F , $F_m = F(y_m) - F(0)$] is plotted as a function of the ratio of the SCR and diffusion lengths χ . Analytical and numerical results show the same trend: F diminishes as χ increases. The first point of the numerical calculations corresponds to a small electric field, which is not the case for the analytical calculations. The inset shows the potential distribution as a function of θ : The potential is zero for $0 < \theta < \theta_0$, increases for $\theta > \theta_0$, and reaches a maximum at $\theta = 180^\circ$.

The drop in potential in the SCR and EDL (in fact, it is a drop in potentials in the region of the electro-osmotic slip, between the points $Y = 0$ and $Y = Y_m$) is presented in Fig. 19. In this region, the drop in potential is formed in the EDL and SCR for the DNS, but in the semianalytical approach the influence of the EDL is neglected and only the influence of the SCR is taken into account.

The SCR is formed in the region $0 < Y < Y_m$; it exists in the area of the incoming ion flux and disappears in the area of the outgoing ion flux. Numerically, Y_m was calculated at the point of maximum space charge ρ and the averaging took place for unsteady DNS calculations. A

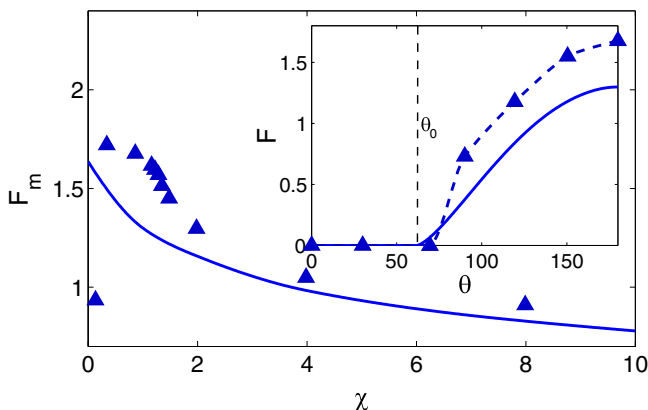


FIG. 19. Normalized drop of the electrical potential F in the region $0 < y < y_m$ as a function of χ at $\theta = 180^\circ$, $F = F_m$, at $\varkappa = 0.26$. The solid line stands for the semianalytical solution and the triangles stand for the numerics. The inset shows F_m along the surface of the granule at $\chi = 1$.

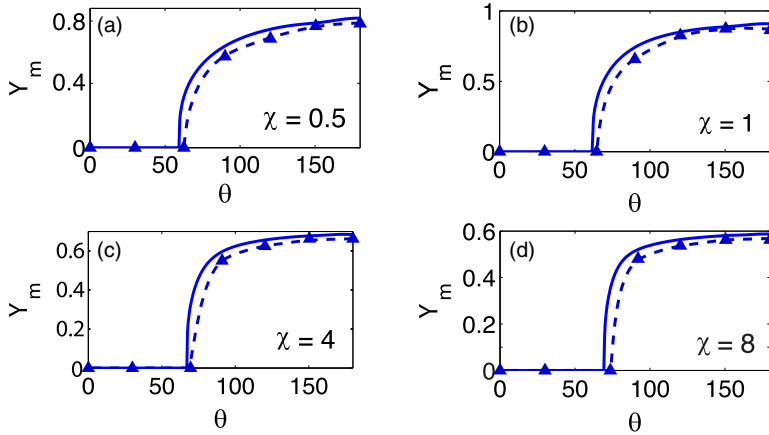


FIG. 20. Length of the SCR, Y_m , at different points of the granule surface. The solid line stands for the semianalytical solution and the triangles joined by the dashed line stand for the numerics.

comparison of Y_m obtained by the semianalytical approach and by the DNS is given in Fig. 20. The DNS shows that the EDL in the area of the outgoing ion flux is zero with graphical accuracy. Again, there is a rather good match between our two approaches.

The ion flux $J(\theta)$ on the microgranule surface is shown in Fig. 21 for several values of χ . One can find a perfect match between the DNS and analytics for the incoming ion flux $J(\theta) > 0$. In contrast, for the outgoing ion flux $J(\theta) < 0$, the discrepancy between two approaches is rather significant. This discrepancy is a consequence of the assumption that we excluded from our analytical analysis the localized ion jet of high conductivity, located just behind the granule, at small angles θ [the existence of such a jet is shown, for example, in Figs. 6(a) and 11(b)]. However, this discrepancy has a small influence on the other unknowns.

The quantity of the most practical interest is the electrophoretic velocity u_∞ . This velocity, normalized by \varkappa and obtained by our semianalytical approach, is plotted as a function of χ in Fig. 22 for two boundary values of \varkappa ; it is located inside a rather narrow shaded area. The coupling coefficient \varkappa for practically important electrolyte solutions lies between these boundary values. The

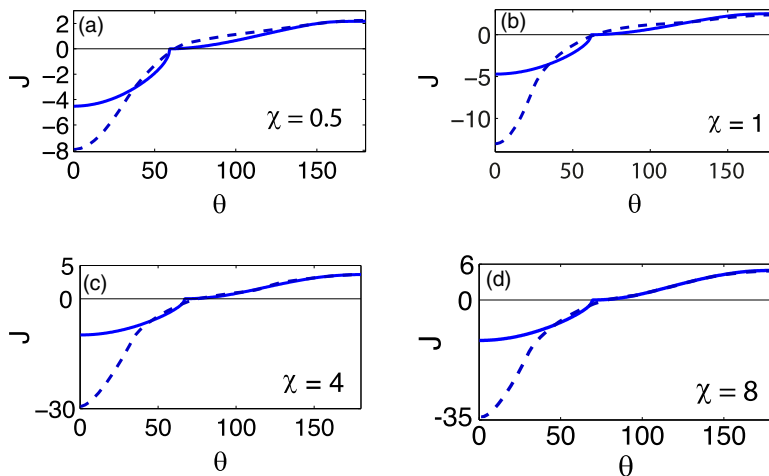


FIG. 21. Ion flux J on the surface versus the angle θ for different χ . The dashed line stands for the DNS results and the solid line stands for the analytics.

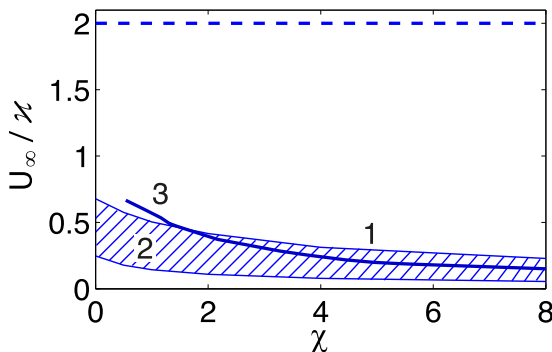


FIG. 22. Electrophoretic velocity according to different theoretical approaches as a function of χ . Curves 1 and 2 are the predictions of our semianalytical theory: 1 stands for $\varkappa = 0.1$ and 2 stands for $\varkappa = 1$. Curve 3 corresponds to the DNS with $\varkappa = 0.26$ and $\nu = 0.002$. The dashed line corresponds to Dukhin's relation (45).

values of U_∞/\varkappa , calculated by the DNS, are also plotted in the figure. There is good agreement between the analytical and numerical approaches except for small values of χ because they belong to the regime of underlimiting currents (the electrophoresis of the first kind, according to Dukhin's terminology).

From physical considerations, Dukhin derived his famous formula for the electrophoresis of the second kind (see Dukhin [7]), which in the dimensional form is

$$\tilde{u}_\infty = 2 \frac{\tilde{\varepsilon} \tilde{a} \tilde{E}_\infty^2}{\tilde{\mu}}. \quad (44)$$

In our dimensionless form, the relation (44) becomes

$$\frac{U_\infty}{\varkappa} = 2. \quad (45)$$

This dependence is plotted in Fig. 22 by the dashed line. We will return to the electrophoretic velocity when we compare the theoretical and experimental data.

The nonstationary terms in the semianalytical formulation appear only from the convection-diffusion equation (32). Thus, only a thin diffusion layer can be unstable. A typical discrete spectrum of eigenvalues is plotted in Fig. 23 for $\chi = 2$. Most of the eigenvalues come in complex-conjugate pairs. Only one such pair is unstable. The eigenfunctions are oscillating and decaying with departure from the pole $\theta = 180^\circ$. Their profiles qualitatively correspond to the ones obtained numerically (see Fig. 15). In Fig. 24, with an increase of χ , the number of unstable modes also increases. With a decrease of χ , the real part of the unstable complex-conjugate pair decreases. Finally, at $\chi < \chi_*$ this mode becomes stable, $\lambda_R < 0$. Note that the unstable mode never becomes a real number.

The dependence of the real part of the most dangerous mode (with maximal real part) λ_R on χ is shown in Fig. 24. The critical χ is, according to analytical evaluation, $\chi_*^a \approx 0.55$; the DNS shows that the stationary mode is replaced by the nonstationary one at $\chi_*^N \approx 1.28$. This difference is attributed to the simplifications in the semianalytical approach.

E. Comparison with experimental data

The results of our DNS and semianalytical analysis are compared with the experimental data. In this work, we analyze the experimental data from the papers by Barany *et al.* [51] and Mishchuk *et al.* [31,33,52] to compare with our theory. The radius of the cation-exchange particle \tilde{a} varied from 0.5 to 600 μm in experiments; the concentration of the NaCl solution for which the comparison was made was taken to be 10^{-4} mol/l. The intensity of the external electric field ranged from 1 V/m to 100 kV/m. Moreover, the ion-selective particles in the experiments were fabricated from

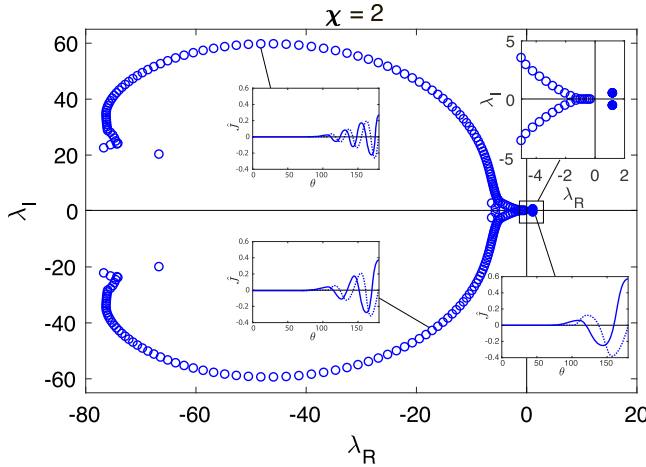


FIG. 23. Typical spectrum of the linear stability problem for the semianalytical solution in the complex λ plane for $\chi = 2$. The top inset shows a conjugate pair of unstable eigenvalues in the vicinity of the origin. The other insets show the real part of eigenfunctions at different points of the spectrum as a function of θ .

various types of material. The ion-selective particle is in fact a spherical membrane, which is an organic polymer consisting of a matrix and pores. For a cation-selective particle, a concentration of fixed and immobile anions is maintained on its surface, which creates a fixed membrane charge p ($c_a = p$). This fixed charge p is accounted for as an empirical parameter, varying with the type of material. If this membrane charge is large enough ($p \gg 1$), then it is more difficult for external forces to change the number of cations inside the membrane [36] and $c^+ = p$ is assumed inside the membrane and at its surface with the electrolyte. From the viewpoint of our approach, changing the particle fabric means changing the cation concentration p at the particle surface $r = 1$ [see the first BC in Eq. (10)]. As we showed in our previous work [36], for the electrophoresis of the second kind, the dependence on p is practically absent (see also Fig. 1). In other words, the dependence on the particle fabric in our comparison was neglected.

The dimensional electro-osmotic velocity \tilde{u}_m along the microgranule is plotted in Fig. 25. The velocity field from DNS was taken at the point \tilde{y}_m . Experimental points were taken from the work by Mishchuk and Takhistov [31]. In the region of the incoming ion flux, the maximum velocity is reached at an angle of $\theta \approx 60^\circ$. The theoretical maximal velocity at this point and the profile of

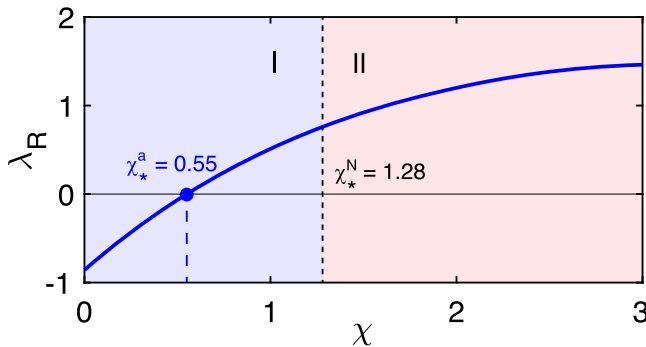


FIG. 24. Maximum growth rate mode λ_R as a function of χ . Here χ_*^a and χ_*^N are analytical and numerical critical values, respectively. Regions I and II correspond to the numerical steady and unsteady regimes, respectively.

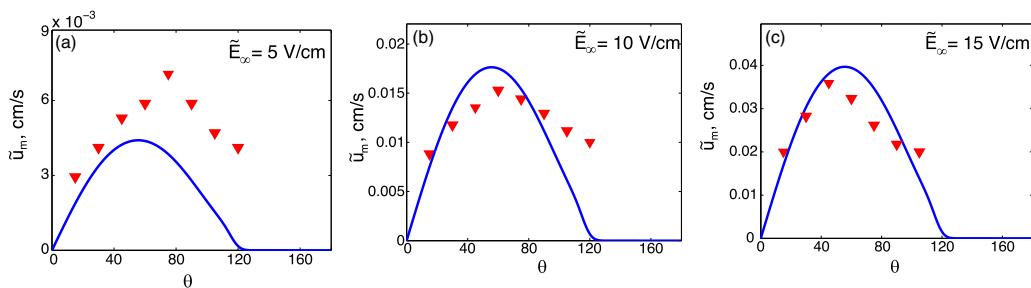


FIG. 25. The solid line stands for the results of our DNS and triangles stand for the experiment [31]. The dimensionless parameter χ is (a) $\chi = 0.035$, (b) $\chi = 0.088$, and (c) $\chi = 0.151$. In these plots the angle is counted in the reverse direction to match the experiments.

the dependence are in good agreement with the experiment. In the region of outgoing ion flux, the electro-osmotic velocity is zero with graphical accuracy, and this velocity could not be captured in the experiment.

For the sake of convenience of comparison with the experiments, we collect the markers for different experimental points in Table II. The dependence of the electrophoretic velocity on the electric field is of the greatest practical interest, so the field strength is added to the table.

To get a better perspective, we present all the experimental points in our dimensionless logarithmical coordinates u_∞ vs E_∞ (see Fig. 26). A region of electrophoresis of the first kind (I) is clearly visible when the velocity is proportional to E_∞ . After the transition region (II), the region of strongly nonlinear electrophoresis (III), as predicted by Dukhin, occurs. According to Dukhin's prediction (44), $u_\infty = 2\chi E_\infty^2$, which corresponds to line 3 in the figure. One can see a deviation of the experimental data from the Dukhin prediction. The dependence $u_\infty \sim \text{const}_2 E_\infty^{4/3}$ is much better suited to the experimental data.

It is instructive to present the normalized experimental and the theoretical electrophoretic velocity $U_\infty = u_\infty/E_\infty^2$ as a function of the universal variable $\chi = \nu^{2/3} E_\infty^{4/3}$. Such a dependence is presented in Fig. 27. Similar to the previous graph, the vertical dashed lines represent the conditional boundaries of the zones of small (I), moderate (II), and high (III) electric field strengths. Our numerical code fails at a sufficiently large electric field and in Fig. 27 the solid line breaks off at $\chi \approx 8$. Meanwhile, the semianalytical solution complements the DNS and can be extended for any large χ . The mismatch between the analytical and numerical solutions at small χ is as much as

TABLE II. Experimental data from different references.

Marker	Radius (μm)	Reference	\tilde{E}_∞ (kV/m)
+	600	[40,51]	2.5–8
•	375	[34,40,51,52]	2.5–30
▼	250	[34,40,51,52]	0.5–100
×	112.5	[51]	10–90
■	100	[34,40,51,52]	0.5–100
▽	62.5	[51]	15–90
□	50	[33,34,40,51,52]	0.5–100
▲	25	[33,34,40,51,52]	2.5–90
△	5	[33,34,40,51,52]	1–10
◇	2.5	[33,34,40,51]	1–10
◆	0.5	[33,34,40,51]	0.2–10

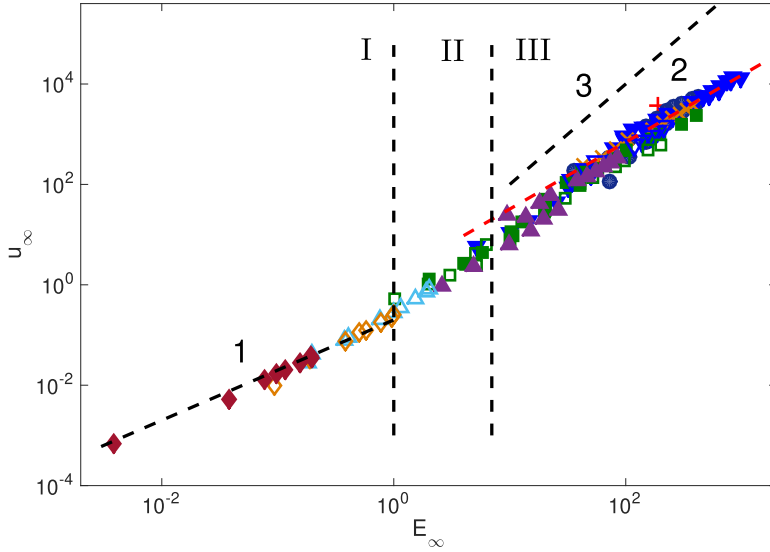


FIG. 26. Experimental dimensionless velocity u_∞ as a function of E_∞ . Here I, II, and III are the region of electrophoresis of the first kind, the transition region, and the region of electrophoresis of the second kind, respectively. Lines 1, 2, and 3 stand for $u_\infty \sim \text{const}_1 E_\infty$, $u_\infty \sim \text{const}_2 E_\infty^{4/3}$, and $u_\infty \sim \text{const}_2 E_\infty^2$, respectively.

twofold, but with increasing χ this difference rapidly decreases practically to zero. At $\chi > 8$, only the analytical method works, and it gives a very good match with the experimental data.

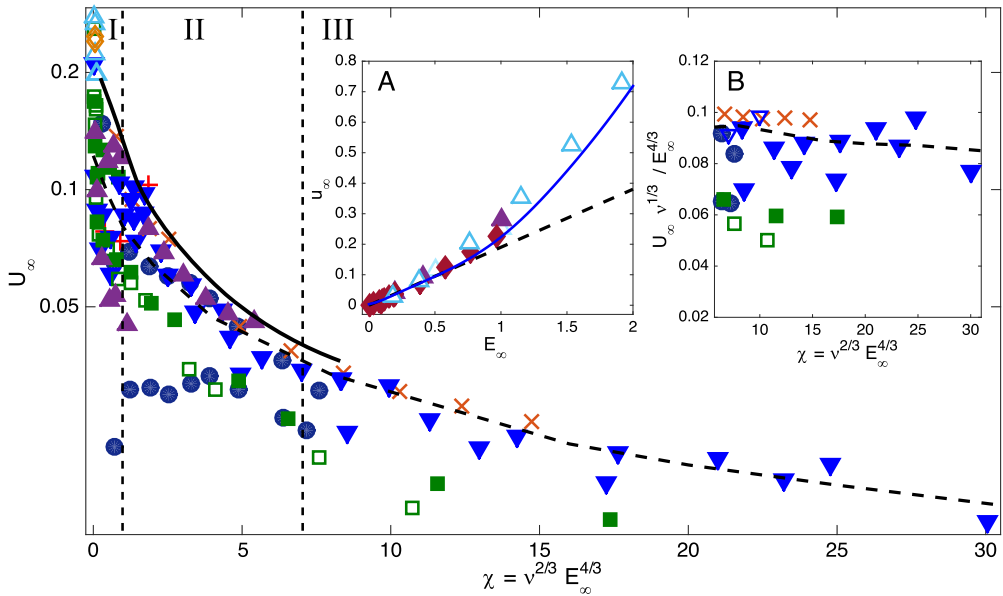


FIG. 27. Comparison of the theoretical and experimental electrophoretic velocities for the universal variables U_∞ vs χ . The markers for the experimental points are given in Table II; the solid line stands for the results of our DNS at $\nu = 0.002$ and the dashed line stands for the semianalytical results. Inset A shows the behavior of u_∞ for small E_∞ . The solid line stands the DNS and the dashed line stands for the analytical solution. Inset B shows the behavior of u_∞ for large E_∞ .

As we have shown previously, the entire semianalytical solution and particularly the electrophoretic velocity strongly depend on the diffusion-convection phenomenon in the diffusion layer. As a result, at the fixed coupling coefficient \varkappa , the normalized electrophoretic velocity U_∞ is a function of the parameter χ ,

$$U_\infty = f(\chi). \quad (46)$$

Our calculations for the semianalytical approach at large χ show that, at $\chi \rightarrow \infty$,

$$U_\infty \sim \frac{1}{\sqrt{\chi}}. \quad (47)$$

Unfortunately, we were unable to derive a simple analytical relation for this kind of asymptotic. In Dukhin's approach, the influence of the diffusion layer is neglected and there is no dependence on χ [see the relationship (45)]. In our opinion, this is the main reason for the mismatch between Dukhin's prediction (45) and the experiments. In the experiments shown in Fig. 27, one can see that U_∞ is not constant at all at $\chi \rightarrow \infty$ but decreases with an increase of χ , which is in full accord with the semianalytical approach. The relation (47) can be also presented in the form

$$U_\infty \sim E_\infty^{-2/3} \quad \text{or} \quad u_\infty \sim E_\infty^{4/3},$$

which is in good agreement with experiments (see inset B of Fig. 27).

IV. CONCLUSION

Electrophoresis of an ion-selective granule in an electrolyte solution was investigated numerically and semianalytically for a small EDL and overlimiting and extremely overlimiting currents. Numerical analysis was fulfilled on the basis of the full nonstationary Nernst-Planck-Poisson-Stokes system with the corresponding BCs, initial conditions, and the condition of a force-free particle. For a not very large external field, at $t \rightarrow \infty$, a steady-state solution was achieved. The structure of this solution in space is rather complicated. In the area of the incoming ion flux, three boundary layers that are nested inside each other are formed: the EDL region, the SCR, and the thin diffusion layer. Only one boundary layer, the EDL, is formed in the area of the outgoing ion flux. A separation of the diffusion boundary layer occurs at the point of zero ion flux. In the area of the outgoing ion flux, this flux generates a jet of high salt concentration. With an increase of the external field this jet becomes narrower, but the salt concentration inside the jet is increased.

At the external electric field above the critical value, the steady-state solution loses its stability with respect to the electrokinetic mode. The instability arises in the diffusion layer region but manifests itself in other regions. In particular, it generates electrokinetic microvortices and eventually two kinds of microvortices can be found: the large steady Dukhin-Mishchuk vortices and the electrokinetic ones that propagate from the pole towards the Dukhin-Mishchuk vortices. At small supercriticality, the oscillations of the unknowns are periodic, but the flow becomes chaotic with an increase of the external field in the Feigenbaum scenario. The typical frequency of oscillations is within the window $\tilde{f} = 0.2\text{--}20$ kHz and the amplitude of the oscillations of the unknowns is small, not more than 6% of the mean solution.

For very large external fields, our numerical analysis fails and thus was accompanied by a sophisticated semianalytical solution of the system at $E_\infty \rightarrow \infty$ and $\nu \rightarrow 0$, but $\nu^{2/3} E_\infty^{4/3} = O(1)$. The solution in the diffusion boundary layer was found to be self-similar and significantly simplified. A nature of the separation of the diffusion layer was understood for this self-similar solution. A linear stability of the steady-state solution was investigated and the fact of its instability against the electrokinetic mode was confirmed.

Theoretical results for the DNS and semianalytical solution were successfully compared with the available experimental data. The experimental electro-osmotic velocity and the electrophoretic velocity are in reasonably good agreement with our theory. Moreover, in the comparison of our theoretical electrophoretic velocity with experiments and the Dukhin relation, we found a

discrepancy between the Dukhin formula in experiments and our theory. We have managed to improve upon this discrepancy.

For very large external fields, our numerical analysis fails and should be accompanied by a semianalytical solution for the system (4)–(15). Such a combination of numerical and analytical solutions has allowed us to get a full description of electrophoresis in the whole range of experiments [7]. A semianalytical solution helps us to better understand the nature of the electrophoresis of an ion-selective particle and also the structure of its sophisticated boundary layers, which are nested inside each other near the microgranule. Nonlinear electrophoresis of ion-selective microparticles was described by a rather complicated set of coupled partial differential equations. The investigation of this challenging open problem constitutes a desired extension of the present analysis.

ACKNOWLEDGMENTS

This work was supported in part by the Russian Foundation for Basic Research, Projects No. 16-08-00643-a and No. 18-58-15004; the Russian Science Foundation, Project No. 17-79-10343; and the French Embassy in Russia through the Vernadski program. The research was carried out using the equipment of the shared research facilities of HPC computing resources at Lomonosov Moscow State University.

APPENDIX: SOLUTION IN THE BULK OUTER REGION IV

We derived a system (39)–(41) of three equations for four unknowns, J , F , Δ , and B . The fourth equation to complete the system will be derived from the solution in the outer region $1 < r < \infty$. In this region, $K = 2$ and the electric potential is described by the Laplace equation

$$\nabla^2 \Phi = 0. \quad (\text{A1})$$

The Laplace equation is complemented by two BCs: at $r = 1$ and $r = \infty$. The BC at $r = 1$ has to be taken from the inner solution. The electric potential Φ in the inner regions is changed from $\Phi = 0$ to $\Phi = F$ at the edge of the diffusion layer. This provides one BC,

$$\Phi = F \quad \text{for } r = 1. \quad (\text{A2})$$

The condition at infinity is determined by the third condition (11), taken in the form

$$\Phi = -\cos \theta \quad \text{for } r \rightarrow \infty. \quad (\text{A3})$$

The solution of this problem has the form

$$\Phi = -r \cos \theta + \int_0^\pi [F(s) + \cos s] \sum_{k=0}^{\infty} \frac{2k+1}{2r^{k+1}} P_k(\cos s) P_k(\cos \theta) \sin s ds, \quad (\text{A4})$$

where $P_k(\cos \theta)$ are the Legendre polynomials.

The relation for the ion flux $j = K \partial \varphi / \partial r + \partial \rho / \partial r$ should be used to get the dependence between J and F . For the electroneutral bulk region with $K = 2$, it yields

$$J = 2 \frac{\partial \Phi}{\partial r} \quad \text{for } r = 1. \quad (\text{A5})$$

The desired relation between J and F is easily deduced from the formulas (A4) and (A5),

$$J = -2 \cos \theta - \int_0^\pi [F(s) + \cos s] \sum_{k=0}^{\infty} (2k+1)(k+1) P_k(\cos s) P_k(\cos \theta) \sin s ds. \quad (\text{A6})$$

The system of equations (39)–(41) and (A6) with BCs (42) is closed with respect to the unknown functions J , F , Δ , and B .

Hydrodynamic part

Let us consider hydrodynamics in the bulk flow, with $\rho = 0$ and $K = 2$. We can now solve the flow problem, consisting of the homogeneous Stokes equations, taken for the stream function Ψ equation (see [49]),

$$D^2(D^2\Psi) = 0, \quad D^2 = \frac{\partial^2}{\partial r^2} + \frac{\sin\theta}{r^2} \frac{\partial}{\partial\theta} \left(\frac{1}{\sin\theta} \frac{\partial}{\partial\theta} \right), \quad (\text{A7})$$

along with the slip condition at $r = 1$,

$$\Psi = 0, \quad \frac{\partial\Psi}{\partial r} = -U_m \sin\theta \quad \text{for } r = 1, \quad (\text{A8})$$

and the far-field velocity condition

$$\frac{\partial\Psi}{\partial\theta} = r^2 U_\infty \sin\theta \cos\theta, \quad \frac{\partial\Psi}{\partial r} = r U_\infty \sin^2\theta \quad \text{for } r \rightarrow \infty. \quad (\text{A9})$$

Since the problem (A7)–(A9) is linear, the solution is convenient to present as a superposition of two solutions $\Psi = \Psi_\infty + \Psi_1$, where Ψ_∞ is a solution with a zero slip $U_m = 0$ and Ψ_1 is a solution with a zero velocity at $r \rightarrow \infty$, $U_\infty = 0$. The first solution has a simple form

$$\Psi_\infty = -U_\infty \left(r^2 - \frac{3}{2}r + \frac{1}{2r} \right) \frac{\sin^2\theta}{2}. \quad (\text{A10})$$

The second solution can be represented in the form

$$\Psi_1 = -(r^2 - 1) \int_0^\pi U_m(s) \sum_{k=1}^{\infty} \frac{k(k+1)(k+2)}{4r^k} Q_k(\cos s) Q_k(\cos\theta) ds, \quad (\text{A11})$$

where $Q_k(\cos\theta)$ are the Gegenbauer polynomials. The distribution of U_m is described by Eq. (24).

The value of U_∞ is not specified *a priori*; rather, it is determined using the constraint of a force-free particle condition (14), taking into account the inner solution. While straightforward, the present flow problem is technically formidable and we deform the integration surface to the outer of the SCR where the bulk description is valid and $\rho = 0$. For a granule without volume forces instead of this constraint, it is convenient to apply the Leal theorem (see [49], relation 4-180): To get a force-free particle, the stream function $\Psi = \Psi_\infty + \Psi_1$ must be orthogonal to the first Gegenbauer polynomial $Q_1 = \cos\theta$. In our case, the consequences of this theorem finally reduce to the dependence

$$U_\infty = -\frac{1}{2} \int_0^\pi U_m(\theta) \sin^2\theta d\theta, \quad (\text{A12})$$

which at fixed \varkappa is a function of χ only.

-
- [1] S. Park, T. Chung, and H. Kim, Ion bridges in microfluidic systems, *Microfluid. Nanofluid.* **6**, 315 (2009).
 - [2] H.-C. Chang and L. Y. Yeo, *Electrokinetically Driven Microfluidics and Nanofluidics* (Cambridge University Press, Cambridge, 2010).
 - [3] M. Napoli, J. C. T. Eijkel, and S. Pennathur, Nanofluidic technology for biomolecule applications: A critical review, *Lab Chip* **10**, 957 (2010).
 - [4] J.-L. Viovy, Electrophoresis of DNA and other polyelectrolytes: Physical mechanisms, *Rev. Mod. Phys.* **72**, 813 (2000).
 - [5] H.-P. Chen, C.-C. Tsai, H.-M. Lee, S.-C. Wang, and H.-C. Chang, Selective dynamic concentration of peptides at poles of cation-selective nanoporous granules, *Biomicrofluidics* **7**, 044110 (2013).

- [6] S. C. Wang, H. H. Wei, H. P. Chen, M. H. Tsai, C. C. Yu, and H. C. Chang, Dynamic superconcentration at critical-point double-layer gates of conducting nanoporous granules due to asymmetric tangential fluxes, *Biomicrofluidics* **2**, 014102 (2008).
- [7] S. S. Dukhin, Electrokinetic phenomena of the second kind and their applications, *Adv. Colloid Interface Sci.* **35**, 173 (1991).
- [8] S. S. Dukhin and N. A. Mishchuk, Intensification of electro dialysis based on electroosmosis of the second kind, *J. Membr. Sci.* **79**, 199 (1993).
- [9] H. Helmholtz, Studien über elektrische grenzsichten, *Ann. Phys. Chem.* **243**, 337 (1879).
- [10] M. Von Smoluchowski, Contribution a la théorie de l'endosmose électrique et de quelques phénomènes corrélatifs, *Bull. Acad. Sci. Cracovie* **8**, 182 (1903).
- [11] A. G. Van Der Put and B. H. Bijsterbosch, Electrical conductivity of dilute and concentrated aqueous dispersions of monodisperse polystyrene particles. Influence of surface conductance and double-layer polarization, *J. Colloid Interface Sci.* **75**, 512 (1980).
- [12] P. H. Wiersema, A. L. Loeb, and J. T. G. Overbeek, Calculation of the electrophoretic mobility of a spherical colloid particle, *J. Colloid Interface Sci.* **22**, 78 (1966).
- [13] R. W. O'Brien and L. R. White, Electrophoretic mobility of a spherical colloidal particle, *J. Chem. Soc. Faraday Trans.* **274**, 1607 (1978).
- [14] M. Z. Bazant, in *Electrokinetics and Electrohydrodynamics in Microsystems*, edited by A. Ramos, CISM Courses and Lectures Vol. 530 (Springer, Vienna, 2011), pp. 221–297.
- [15] J. Lyklema, *Fundamentals of Interface and Colloid Science. Volume II: Solid-Liquid Interfaces* (Academic, San Diego, 1995).
- [16] M. Hamed and E. Yariv, Induced-charge electrokinetic flows about polarizable nano-particles: The thick-Debye-layer limit, *J. Fluid Mech.* **627**, 341 (2009).
- [17] E. Yariv, An asymptotic derivation of the thin-Debye-layer limit for electrokinetic phenomena, *Chem. Eng. Commun.* **197**, 3 (2010).
- [18] E. Yariv and A. M. J. Davis, Electro-osmotic flows over highly polarizable dielectric surfaces, *Phys. Fluids* **22**, 052006 (2010).
- [19] G. Yossifon, I. Frankel, and T. Miloh, Symmetry breaking in induced charge electro-osmosis over polarizable spheroids, *Phys. Fluids* **19**, 068105 (2007).
- [20] O. Schnitzer and E. Yariv, Dielectric-solid polarization at strong fields: Breakdown of Smoluchowski's electrophoresis formula, *Phys. Fluids* **24**, 082005 (2012).
- [21] O. Schnitzer and E. Yariv, Macroscale description of electrokinetic flows at large zeta potentials: Nonlinear surface conduction, *Phys. Rev. E* **86**, 021503 (2012).
- [22] O. Schnitzer, R. Zeyde, I. Yavneh, and E. Yariv, Weakly nonlinear electrophoresis of a highly charged colloidal particle, *Phys. Fluids* **25**, 052004 (2013).
- [23] I. Rubinstein and L. Shtilman, Voltage against current curves of cation exchange membranes, *J. Chem. Soc. Faraday Trans.* **75**, 231 (1979).
- [24] I. Rubinstein and B. Zaltzman, Electro-osmotically induced convection at a permselective membrane, *Phys. Rev. E* **62**, 2238 (2000).
- [25] B. Zaltzman and I. Rubinstein, Electro-osmotic slip and electroconvective instability, *J. Fluid Mech.* **579**, 173 (2007).
- [26] E. A. Demekhin, V. S. Shelistov, and S. V. Polyanskikh, Linear and nonlinear evolution and diffusion layer selection in electrokinetic instability, *Phys. Rev. E* **84**, 036318 (2011).
- [27] E. A. Demekhin, N. V. Nikitin, and V. S. Shelistov, Direct numerical simulation of electrokinetic instability and transition to chaotic motion, *Phys. Fluids* **25**, 122001 (2013).
- [28] E. A. Demekhin, N. V. Nikitin, and V. S. Shelistov, Three-dimensional coherent structures of electrokinetic instability, *Phys. Rev. E* **90**, 013031 (2014).
- [29] V. S. Pham, Z. Li, K. M. Lim, J. K. White, and J. Han, Direct numerical simulation of electroconvective instability and hysteretic current-voltage response of a permselective membrane, *Phys. Rev. E* **86**, 046310 (2012).
- [30] C. L. Druzgalski, M. B. Andersen, and A. Mani, Direct numerical simulation of electroconvective instability and hydrodynamic chaos near an ion-selective surface, *Phys. Fluids* **25**, 110804 (2013).

- [31] N. A. Mishchuk and P. V. Takhistov, Electroosmosis of the second kind, *Colloids Surf. A* **95**, 119 (1995).
- [32] N. O. Barinova, N. A. Mishchuk, and T. A. Nesmeyanova, Electroosmosis at spherical and cylindrical metal surfaces, *Colloid J.* **70**, 695 (2008).
- [33] N. A. Mishchuk and N. O. Barinova, Theoretical and experimental study of nonlinear electrophoresis, *Colloid J.* **73**, 88 (2011).
- [34] S. Barany, Electrophoresis in strong electric fields, *Adv. Colloid Interface Sci.* **147-148**, 36 (2009).
- [35] E. Yariv, Migration of ion-exchange particles driven by a uniform electric field, *J. Fluid Mech.* **655**, 105 (2010).
- [36] E. A. Frants, G. S. Ganchenko, V. S. Shelistov, S. Amiroudine, and E. A. Demekhin, Nonequilibrium electrophoresis of an ion-selective microgranule for weak and moderate external electric fields, *Phys. Fluids* **30**, 022001 (2018).
- [37] B. Levich, *Physicochemical Hydrodynamics* (Prentice Hall, Englewood Cliffs, 1962).
- [38] S. S. Dukhin, N. A. Mishchuk, and P. B. Takhistov, Electroosmosis of the second kind and unrestricted current increase in the mixed monolayer of an ion-exchanger, *Colloid J. USSR* **51**, 540 (1989).
- [39] Y. Ben, E. A. Demekhin, and H.-C. Chang, Nonlinear electrokinetics and “superfast” electrophoresis, *J. Colloid Interface Sci.* **276**, 483 (2004).
- [40] S. Barany, N. A. Mishchuk, and D. C. Prieve, Superfast electrophoresis of conducting dispersed Particles, *J. Colloid Interface Sci.* **207**, 240 (1998).
- [41] S. J. Kim, Y.-C. Wang, J. H. Lee, H. Jang, and J. Han, Concentration Polarization and Nonlinear Electrokinetic Flow near a Nanofluidic Channel, *Phys. Rev. Lett.* **99**, 044501 (2007).
- [42] H.-C. Chang, G. Yossifon, and E. A. Demekhin, Nanoscale electrokinetics and microvortices: How microhydrodynamics affects nanofluidic ion flux, *Annu. Rev. Fluid Mech.* **44**, 401 (2012).
- [43] See Supplemental Material at <http://link.aps.org/supplemental/10.1103/PhysRevFluids.4.043703> for details.
- [44] V. S. Shelistov, E. A. Demekhin, and G. S. Ganchenko, Self-similar solution to the problem of electrokinetic instability in semipermeable membranes, *Moscow Univ. Mech. Bull.* **69**, 119 (2014).
- [45] H.-C. Chang, E. A. Demekhin, and V. S. Shelistov, Competition between Dukhin’s and Rubinstein’s electrokinetic modes, *Phys. Rev. E* **86**, 046319 (2012).
- [46] P. Glendinning, *Stability, Instability and Chaos* (Cambridge University Press, Cambridge, 1994).
- [47] M. J. Feigenbaum, Universal behavior in nonlinear systems, *Los Alamos Sci.* **1**, 4 (1980) [reprinted in H. Bai-Lin, *Chaos* (World Scientific, Singapore, 1984)].
- [48] V. I. Arnold, *Geometrical Methods in the Theory of Ordinary Differential Equations* (Springer, Berlin, 1983).
- [49] L. G. Leal, in *Laminar Flow and Convective Transport Processes: Scaling Principles and Asymptotic Analysis*, edited by H. Brenner (Butterworth-Heinemann, Oxford, 1992).
- [50] J. G. F. Francis, The QR transformation a unitary analogue to the LR transformation—Part 1, *Comput. J.* **4**, 265 (1961).
- [51] A. A. Baran, Y. A. Babich, A. A. Tarovsky, and N. A. Mishchuk, Superfast electrophoresis of ion-exchanger particles, *Colloid. Surf.* **68**, 141 (1992).
- [52] N. A. Mishchuk and S. S. Dukhin, in *Interfacial Electrokinetics and Electrophoresis*, edited by Á. V. Delgado (Dekker, New York, 1992).